


# Effects of roughness on the turbulent Prandtl number, timescale ratio, and dissipation of a passive scalar

Zvi Hantsis  and Ugo Piomelli\**Department of Mechanical and Materials Engineering, Queen's University, Kingston, Ontario, Canada K7L 3N6*

(Received 9 June 2022; accepted 14 November 2022; published 12 December 2022)

The transport of a passive scalar with molecular Prandtl number  $Pr$  near unity was studied using direct numerical simulations (DNS) of a fully developed channel with smooth and rough walls. The effects of roughness on the turbulent Prandtl number  $Pr_T$ , turbulent timescale ratio and scalar-dissipation budget were investigated. For the rough-wall case, the turbulent Prandtl number was almost constant ( $Pr_T \approx 0.9$ ) from the roughness centroid up to the roughness crest, matching the common assumption used in modeling.  $Pr_T$  changes rapidly as the base of the roughness is approached, similar to the near-wall behavior in the viscous sublayer of a smooth-wall case. Away from the wall, Townsend's similarity hypothesis holds; the curves collapse when scaled in wall units. An effective turbulent Prandtl number  $Pr_{T,eff}$ , which also includes the dispersive terms was examined.  $Pr_{T,eff}$  and  $Pr_T$  have an overall similar behavior, suggesting that they can be interchangeable and that the  $Pr_T \approx 0.9$  approximation may be accurate enough when modeling rough-wall flows with constant scalar wall flux. This implies that the *ad hoc* adjustment of model coefficients is not necessary, and that the scalar dispersive term do not need to be modeled separately. The near-wall behavior of the ratio between turbulent scalar and momentum timescales,  $\mathcal{R}$ , depends strongly on the molecular  $Pr$  for a smooth-wall case; roughness significantly reduces this dependence, tends to lower  $\mathcal{R}$ , and results in a more uniform behavior. Only below the centroid  $\mathcal{R}$  rises rapidly as the base of the roughness is approached; as  $Pr$  decreases, the location at which this rise occurs approaches the base of the roughness. Townsend's similarity hypothesis also applies to  $\mathcal{R}$  away from the roughness crest. The budget of the scalar dissipation  $\varepsilon_\theta$  has a complex near-wall behavior in a smooth-wall case. In a rough-wall case this behavior is significantly simpler, approximating an equilibrium in which several production-of-dissipation terms match the dissipation-of-dissipation. The leading turbulent production-of-dissipation term is only due to the gradients of velocity and scalar fluctuations, which are only indirectly affected by the roughness. Compared with the smooth-wall case, this term is enhanced due to improved alignment between the fluctuating scalar gradient and the principal compressive direction of the strain-rate tensor. The roughness also enhanced the gradient-production of scalar dissipation, which is directly affected by the roughness shape, due to the diffusive nature of the mean scalar, which results in large gradients of the time-averaged scalar field.

DOI: [10.1103/PhysRevFluids.7.124601](https://doi.org/10.1103/PhysRevFluids.7.124601)

## I. INTRODUCTION

Turbulent flows are present in most applications in engineering and the natural sciences, and accurate models are needed for their analysis. With advances in computational power the use of direct

\*ugo@queensu.ca

numerical simulations (DNS) and large-eddy simulations (LES) has become more widespread. Their general use, however, is still limited by the significant computational resources required by these techniques. The resolution of the region close to a solid wall, in particular, poses significant demands on a computation, which become even more extreme if the surface is rough. Roughness is present in many important applications (if the Reynolds number is large enough, in fact, then any surface is rough), and accounting for its effects is becoming increasingly important. The resolution of the roughness elements on a solid surface is, however, prohibitively expensive for realistic Reynolds numbers [1]. Additional transport equations must be solved if scalar transport (active or passive) has to be included, further increasing the computational demands.

Despite the significant increase in computing power, which bring LES and DNS closer to the practical domain, real-life, complex applications still require experiments, engineering correlations, or simpler models such as the solution of the Reynolds-averaged Navier-Stokes (RANS) equations. Within the context of the RANS approach, most commonly used closure models are of the eddy-viscosity and eddy-diffusivity type. The most common ones are one-equation models (the most popular of these being the Spalart-Allmaras model [2]), two-equation models, where two additional differential transport equations are solved to obtain a length- and velocity-scale [3–5], and Reynolds-Stress models [6] that estimate all the fluctuating stress components.

Attempts to treat roughness in RANS models include modifications to existing models through boundary-conditions (usually through defining a virtual wall where the turbulent kinetic energy (TKE) is nonzero), changing the wall value of various turbulent quantities, or modification of terms in the model equations [4,7], or of the wall functions [8]. A more detailed review of these can be found in Refs. [9,10].

A useful tool in the study of the effects of roughness is the “double-averaging” technique [11], which will be discussed further in Sec. II C, and is based on a combination of time- and space-averaging. Near the roughness the time-averaged fields (velocity, scalar, etc.) vary spatially and differ from the time-and-space-averaged value; the deviation of the time-averaged field from the time-and-space-averaged one, known as “wake field” or “form-induced perturbation,” allows to isolate the direct effects of the geometry. By applying the double-average, additional “form-induced” (FI) terms appear in the transport equations and budgets. For example new FI stresses, referred to dispersive stresses, appear in the averaged momentum equation; similarly, new dispersive fluxes appear in the averaged scalar transport equation [11,12].

Most turbulence models for scalar transport are analogous to those used for momentum transport.<sup>1</sup> Often eddy viscosity  $\nu_T$  and eddy diffusivity  $\alpha_T$  are related by simple algebraic relations, or additional equations for the transport of scalar variance and scalar dissipation are used, of the same form as the momentum closure models with different coefficients. For example, Refs. [13–15] introduced models that add two additional equations for scalar variance  $\mathcal{K}_\theta$  and scalar dissipation  $\varepsilon_\theta$ ; both scalar model equations mirror the transport equations for the TKE  $\mathcal{K}$  and dissipation  $\varepsilon$  used in the momentum closure.

In the context of smooth-wall flows, models employing a two-equation closure for the scalar quantities (such as  $\mathcal{K}_\theta$ - $\varepsilon_\theta$ ) have shown success, in particular due to sufficient similarities between the scalar and momentum fields in the absence of strong pressure gradients [16–20]. Additional quantities are required in these models, the main ones being the turbulent Prandtl number<sup>2</sup>  $\text{Pr}_T$  (the ratio between eddy-viscosity  $\nu_T$  and eddy-diffusivity  $\alpha_T$ ), and the ratio between the integral timescales of velocity and scalar  $\mathcal{R}$ , often referred to as the “scalar-to-mechanical timescale ratio.”

<sup>1</sup>In incompressible flows heat transfer, mass transfer, or the transport of any other passive scalar are equivalent; for simplicity we usually adopt the terminology used for heat transfer, but use it interchangeably with general scalar transport throughout this work. The generic scalar will be denoted by  $\theta$ , its fluctuations by  $\theta'$ .

<sup>2</sup>For passive scalars, the turbulent Prandtl number, turbulent Schmidt number, etc., are equivalent.

The turbulent Prandtl number  $Pr_T$ , plays an essential role in most empirical correlations and eddy-diffusivity models.  $Pr_T$  is analogous to the molecular Prandtl number  $Pr$ , but is a function of the flow conditions rather than a property of the fluid [21].  $Pr_T$  can be used to determine the eddy-diffusivity directly from the eddy-viscosity (usually in conjunction with algebraic or two-equations models for  $\nu_T$ ), to determine the coefficients in more complex models, such as  $\mathcal{K}$ - $\varepsilon$ - $\mathcal{K}_\theta$ - $\varepsilon_\theta$ -type models [13,14,22], or to calculate the dispersive fluxes from the dispersive stresses [23].

A significant amount of work has been devoted to determining  $Pr_T$  in a variety of flows, with particular interest in wall-bounded flow [24]. Kays [16] clarified the usefulness and effectiveness, as well as the limitations, of using  $Pr_T$ . He summarized the different approaches used to calculate  $Pr_T$  by collecting a wide range of sources (analytical, experimental and numerical) for canonical flows such as boundary layers, pipes, and channels. For commonly used engineering applications (such as heat exchanges),  $Pr_T$  is estimated via empirical or semiempirical relations. A core conclusion reached by these studies is that  $Pr_T$  becomes effectively constant in the logarithmic region near the wall and its value is primarily a function of  $Re$  and  $Pr$ . In particular, when  $Pr$  is near unity,  $Pr_T$  approaches a value of about 0.85–0.9 and can be assumed constant for high enough  $Re$  [18,21,25–27]. However, the same studies show that when approaching the wake region of a boundary layer, the centerline of channels or the axis of pipes,  $Pr_T$  decreases to values in the neighbourhood of 0.5. Many models assume a constant value for  $Pr_T$ , despite the fact that this is only justified for the logarithmic region.

Relatively little attention has been given to  $Pr_T$  in the context of rough-wall flows [28–33]. Of these, Kuwata [33] introduced the “effective turbulent Prandtl number”  $Pr_{T,\text{eff}}$ , an approach that extends  $Pr_T$  to include the dispersive stresses and fluxes. They noted that  $Pr_{T,\text{eff}}$  behaves similarly to  $Pr_T$  outside of the roughness sublayer, but increases rapidly inside it.

Compared with  $Pr_T$ ,  $\mathcal{R}$  exhibits a much smaller variation with wall distance [19,34]. For example, in a smooth-wall channel with  $Pr = 0.71$ ,  $\mathcal{R} \approx 0.5$  through most of the channel height; as  $Re$  increases, the near-wall region where  $\mathcal{R}$  differs from this value becomes thinner. Beguier *et al.* [35] observe that  $\mathcal{R} \approx 0.5$  when the velocity and thermal fields are in local equilibrium. The dissipation of scalar variance,  $\varepsilon_\theta$ , is often calculated assuming a constant  $\mathcal{R}$  [36]. The use of  $\mathcal{R}$  is particularly common in the field of combustion; a detailed discussion of this topic can be found in Ref. [37]. However,  $\mathcal{R}$  is harder to calculate from experiments and depends on  $Pr$ .

Little work has been done to determine how these quantities are affected by roughness. Chedevigne [23] cited the lack of data on both  $\mathcal{R}$  and the relation between  $\mathcal{K}$  and  $\mathcal{K}_\theta$  in rough-wall flows as the reason for not implementing a direct model of the dispersive scalar fluxes, following the approach he used for modeling the dispersive stresses. Instead, he estimated the dispersive fluxes from the dispersive stresses (Eq. (27) of Ref. [23]) using an assumption that the ratio  $\mathcal{K}/\mathcal{K}_\theta$  is proportional to the ratio of averaged velocity to averaged scalar.

In addition to using  $Pr_T$  and  $\mathcal{R}$ , several models calculate  $\alpha_T$  directly using additional equations for the transport of the scalar variance  $\mathcal{K}_\theta$  and its dissipation  $\varepsilon_\theta$ .  $Pr_T$  is often used to determine some of the coefficients.  $\mathcal{R}$  is also needed when the scalar dissipation rate  $\varepsilon_\theta$  needs to be directly expressed. This can be achieved either by using the definition of  $\mathcal{R}$  and solving for  $\varepsilon_\theta$  or as part of the transport equation of  $\varepsilon_\theta$  [15,34,38,39].

The budget of TKE has been widely studied for flows over rough surfaces, from rod-roughened channel to vegetation canopies. For example, Refs. [12,40–43] and others examined the TKE budget and spatial distribution, as well as the roughness-associated production mechanisms. Furthermore, the role of the form-drag in the conversion of mean kinetic energy (MKE) to TKE was clarified.

The budget of the scalar variance over rough walls, however, received significantly less scrutiny: Coppin and Raupach [44] used a model plant canopy, showing that the peak  $\mathcal{K}_\theta$  production occurs near the top of the canopy; significant portion of  $\mathcal{K}_\theta$  is then convected into the canopy, to be dissipated. Miyake *et al.* [45] and Nagano *et al.* [46] numerically simulated channels with two-dimensional rods on one of the walls; they observed that the production of  $\mathcal{K}_\theta$  is reduced on the rough-wall compared with the smooth one, resulting in a lower intensities of temperature fluctuations on the rough wall. Recently, Hantsis, and Piomelli [47] examined the budget of the

scalar variance  $\mathcal{K}_\theta$  for Prandtl numbers near unity, focusing on the contribution of the FI production. Comparing the budget of  $\mathcal{K}_\theta$  with that of the streamwise Reynolds stress, they found that the FI production of scalar variance was more significant than that of the streamwise stress, and that the pressure-work term of the streamwise stress caused dissimilarity between the two budgets. It should be noted that models for the transport of  $\mathcal{K}_\theta$  are analogous to those for the  $\mathcal{K}$ , and, because of the absence of the pressure-strain term, the  $\mathcal{K}_\theta$  budget is expected to be more similar to that of  $\mathcal{K}$  than to that of the streamwise stress.

The budget of  $\varepsilon_\theta$  has received significantly less attention, despite the fact that  $\varepsilon_\theta$  plays a crucial role in combustion, where it directly affects the rate of chemical reactions, propagation speed of a flame front, etc. It also controls the rate of scalar mixing (of contaminants, chemical species and heat) and understanding its behavior is essential for optimization of mixing processes.

Experimental and numerical studies have examined the budget of  $\varepsilon_\theta$  in canonical flows, such as isotropic turbulence, shear flows far from solid boundaries [39,48–51]. Abe *et al.* [18] simulated a smooth-wall channel and studied the dissipation budgets of TKE and scalar variance, and reported some differences between the two budgets, as the corresponding terms in scalar and momentum budgets exhibited different magnitudes and near-wall behavior;. These results were corroborated by Alcántara-Ávila *et al.* [20] and Alcántara-Ávila and Hoyas [52]. Abe *et al.* [18] also noted that the similarity between the spectra corresponding to the enstrophy and scalar dissipation rate was not as good as that between the kinetic energy and scalar variance, suggesting that, while a direct analogy between  $\mathcal{K}$  and  $\mathcal{K}_\theta$  is reasonable, the same cannot be said for  $\varepsilon$  and  $\varepsilon_\theta$ . To our knowledge, no study has examined the roughness effects on the scalar dissipation budget.

When  $\varepsilon_\theta$  is used to calculate an eddy diffusivity, its transport equation is not based on the exact one, but rather on phenomenological observations and physical reasoning. Nevertheless, the model equation still needs to conform with the physics of  $\varepsilon_\theta$ , at least in a general sense. Since the introduction of roughness limits the extent to which the scalar models and rough-wall corrections can be directly drawn from the momentum ones, an analysis of  $\varepsilon_\theta$  for the rough-wall case can be beneficial. In addition, the FI terms caused by the roughness have never been considered. However, an understanding of their behavior can be critical in developing more advanced turbulence models such as DANS [23], which requires modeling of the dispersive stresses and dispersive scalar fluxes.

The motivation of the study is to provide modelers with information that can help extend well-known two-equation scalar models to apply to rough-wall cases. The effects of roughness enter the model equations through the changes to  $\text{Pr}_T$  and  $\mathcal{R}$ , but also from the presence of FI terms in the transport equations; these terms should, ideally, be accounted for in the models. This paper, therefore, will first consider  $\mathcal{R}$  and  $\text{Pr}_T$ , and then focus on the budget of  $\varepsilon_\theta$  and  $\mathcal{K}_\theta$ , the latter mostly from a modeling point of view.

The following sections will describe the mathematical description of the test case, the numerical setup, and details about important quantities that are used throughout this work. Then, results will be presented for  $\text{Pr}_T$  and  $\text{Pr}_{T,\text{eff}}$ , the timescale ratio  $\mathcal{R}$ , the budgets of  $\mathcal{K}$  and  $\mathcal{K}_\theta$ , and finally on the budget of  $\varepsilon_\theta$ . Concluding remarks will close the paper.

## II. MATHEMATICAL MODEL

### A. Problem definition

A summary of the problem setup will be presented here. A more detailed description of the methodology can be found in Ref. [47]; here we only recall the salient points. We consider the transport of a passive scalar in a fully developed turbulent channel with rough walls. The flow is driven by a mean streamwise pressure gradient in a periodic domain and a constant scalar flux is maintained through the walls, as was considered by other authors [27,32,36,53,54]. The ratio of molecular viscosity  $\nu$  to molecular diffusivity  $\alpha$  defines the molecular Prandtl number  $\text{Pr} = \nu/\alpha$ . We focus on  $\text{Pr} = 1.0$ , although we also include results for  $\text{Pr} = 0.7$  when appropriate; overall the two cases are very similar and when differences exist they are specifically addressed.

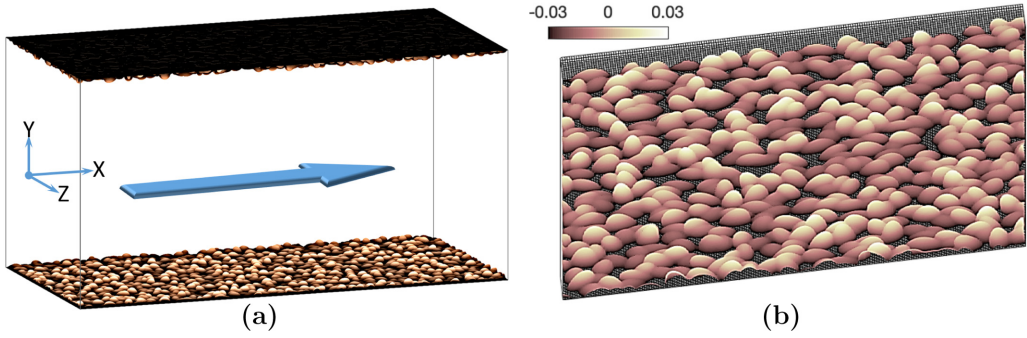


FIG. 1. (a) Sketch of the computational domain. The arrow indicates the flow direction. (b) Detail of the roughness geometry and mesh size. The color indicates the wall-normal distance relative to the virtual wall ( $y - d = 0$ ).

The transport of momentum is governed by the incompressible Navier-Stokes equations and mass conservation:

$$\frac{\partial u_k}{\partial x_k} = 0, \quad (1)$$

$$\frac{\partial u_i}{\partial t} + \frac{\partial (u_i u_k)}{\partial x_k} = \Pi \delta_{i1} - \frac{\partial p}{\partial x_i} + \nu \nabla^2 u_i + F_i, \quad (2)$$

where  $x_i$  (or  $x$ ,  $y$ , and  $z$ ) are the Cartesian coordinates in the streamwise, wall-normal, and spanwise directions, respectively.  $u_i$  (or  $u$ ,  $v$ , and  $w$ ) are the velocity components in the Cartesian directions,  $p = P/\rho$  is the pressure divided by the (constant) density,  $F_i$  is a forcing term used by the immersed boundary method (IBM) to impose the roughness geometry in the Cartesian domain.  $\Pi$  is the driving pressure gradient, adjusted in time to maintain a constant mass flux through the channel. No-slip conditions are used at the wall, while periodicity is enforced in the streamwise and spanwise directions.

Given a passive scalar  $T$  with wall value  $T_w$ , we define the transformed scalar  $\theta \equiv T_w - T$ . Following the approach of Ref. [53], which has been used extensively in the literature [27,32,36,54], the governing equation for the transformed passive scalar is

$$\frac{\partial \theta}{\partial t} + \frac{\partial (u_k \theta)}{\partial x_k} = \alpha \nabla^2 \theta + Q + F_\theta; \quad (3)$$

here, the forcing term  $Q$  is

$$Q = u \frac{dT_w}{dx} = \frac{q_w}{\rho c_p \delta} \frac{u}{U_b}, \quad (4)$$

where  $c_p$  is the specific scalar capacitance (i.e., specific heat, specific moisture, etc.),  $U_b$  is the bulk velocity,  $\delta$  is the channel half-width, and  $q_w$  is the prescribed scalar wall flux.

The roughness is  $k$  type and is modeled, following Scotti [55], as a random distribution of ellipsoids with axes in the proportion  $k:1.4k:2k$ . The roughness crest is located at  $y_{cr} \approx 1.5k$  and  $k = 0.04\delta$  (where  $\delta$  is the channel half-height); this value allows us to minimize blockage effects, while reaching the fully rough regime. An immersed-boundary method (IBM) based on the volume-of-fluid (VoF) approach is used to represent the geometry within a cartesian mesh [55].  $\delta$  and the bulk velocity  $U_b$ , can be used to define the bulk Reynolds number  $Re_b = U_b \delta / \nu$ . All calculations are performed with  $Re_b = 21\,000$ , resulting in a Reynolds number based on friction velocity  $u_\tau$  of  $Re_\tau \simeq 1020$  for the smooth-wall case and  $Re_\tau \simeq 1700$  for the rough-wall one. The channel and roughness geometries are shown in Fig. 1.



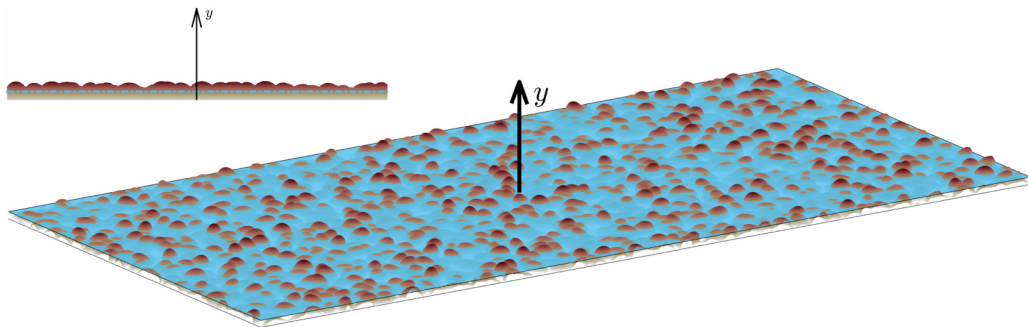


FIG. 2. Illustration of the virtual wall plane (light blue) located at the roughness centroid at  $y - d = 0$ . Inset shows a zoomed-in view of the  $XY$  plane with the  $y$  axis origin. Roughness is coloured based on the distance from the base of the roughness at  $y = 0$ .

For the smooth case,  $1024 \times 320 \times 512$  grid points are used to discretize a domain of dimensions  $6\delta \times 2\delta \times 3\delta$ , and  $1024 \times 530 \times 512$  are employed in the rough one. Note that in the latter case, the actual domain height is  $2.064\delta$  (rather than  $2\delta$ ) to compensate for the blockage due to the roughness. This results in  $\Delta x^+ = \Delta z^+ \simeq 6$  in the smooth case, and 10 in the rough one. The resolution of the roughness is  $n_x = n_z = 7$  cells per  $k$  in the  $x$  and  $z$  directions while in the  $y$  direction there are  $n_y = 85$  cells per  $k$  and a total of  $n_{\text{crest}} = 125$  cells covering the region from trough to crest. A grid-convergence study was also carried out. A mesh coarser by roughly 25% in all directions showed less than 3% difference for the mean scalar and velocity and less than 5% for the other quantities inspected. The present calculations are in very good agreement with reference data (mean velocity, Reynolds stresses, and TKE budgets) in the two cases considered, as discussed in Ref. [47]. Full details can be found in the Appendix of Hantsis and Piomelli [47].

While the domain is smaller than that used by Lee and Moser [56] or Hoyas and Jiménez [57] ( $8\pi\delta \times 2\delta \times 3\pi\delta$ ), it is similar to that used by Alcántara-Ávila *et al.* [20] ( $2\pi\delta \times 2\delta \times \pi\delta$ ) and is significantly larger than in simulations that use minimal channels to study the near-wall region [58,59]. Alcántara-Ávila *et al.* [20] showed that a domain of this size was large enough to compute accurately first-order statistics and turbulent budgets for a similar combinations of  $\text{Re}_\tau$  and Pr. Townsend’s outer-layer similarity hypothesis [60] (which states that some distance outside of the roughness sublayer, turbulent statistics are independent of the roughness when properly normalized) has been widely confirmed [61,62]. Since we will concentrate on the near-wall region of a two-dimensional plane channel, even if the outer outer layer may be slightly affected by the domain size, the inner-layer statistics are expected to be accurate.

### B. Virtual-wall location

Since the roughness displaces the flow upwards, the effective half-height of the channel is the distance between the channel’s center plane and the mean height of the momentum absorption by the roughness surface [1,63]. This means that the line-of-action of the resultant drag force on the roughness is located at a distance  $d$  from the base of the roughness (trough) given by

$$d = \frac{1}{y_{\text{cr}}} \int_0^{y_{\text{cr}}} F_1 dy, \quad (5)$$

where  $F_1$  is the total force applied on the roughness in the streamwise direction Eq. (2). By definition,  $d \leq y_{\text{cr}}$ ; for a smooth-wall case  $d = 0$ .

The location  $y = d$  is referred to as the “force centroid” or “roughness centroid,” and the horizontal plane  $y = d$  will be referred to as the “virtual wall,” as illustrated in Fig. 2. As mentioned in the previous section, the channel half-width in the rough-wall case is slightly increased to balance

the blockage due to the roughness. This increase of channel half-width is equal to  $d$ ; the distance between the top and bottom virtual walls remains  $2\delta$ , as in the smooth-wall case. More details can be found in Hantsis and Piomelli [47].

### C. Triple decomposition and form-induced quantities

In rough-wall flows, in addition to the usual Reynolds-averaging operator, a second type of averaging can be defined, the triple decomposition [11,12]. Any flow quantity  $f$  can be decomposed into three terms: (1) a component that is averaged both in time and space (or *double-averaged*),  $\langle \bar{f} \rangle$ ; (2) the spatial variation of the time-averaged quantity,  $\bar{f}$ ; and (3) the instantaneous fluctuation  $f'$ :

$$f(x_i, t) = \bar{f}(x_i) + f'(x_i, t) = \langle \bar{f} \rangle(y) + \tilde{f}(x_i) + f'(x_i, t). \quad (6)$$

$\tilde{f}$  is known as the “wake field,” or “form-induced perturbation,” and represents the deviation of the time-averaged field from the double-averaged (time-and-space) one, thus highlighting the geometry-induced effects. The wake-field is a stationary spatial perturbations field, nonzero whenever the time-averaged field is nonuniform.

We utilize two types of spatial averages over the  $xz$  plane: The “intrinsic” spatial average  $\langle \cdot \rangle$ , used in Eq. (6), is only applied to the area  $A_f$  occupied by the fluid within the given horizontal plane while the “superficial” average  $\langle \cdot \rangle_s$  is applied over the entire plane area ( $A_o$ ), including the solid area [11]:

$$\langle f \rangle = \frac{1}{A_f} \iint_{A_f} f dA, \quad \langle f \rangle_s = \frac{1}{A_o} \iint_{A_o} f dA. \quad (7)$$

The fluid fraction  $\phi(y) = A_f/A_o$ , i.e., the ratio of fluid area to total area, directly relates the two averages:  $\langle \cdot \rangle_s = \phi \langle \cdot \rangle$ . By definition,  $\langle \tilde{\cdot} \rangle = \langle \tilde{\cdot} \rangle_s = 0$  and, if the time-averaged fields are spatially uniform (in  $x$  and  $z$ )  $\tilde{\cdot} = 0$ , the triple decomposition reverts back to the standard Reynolds decomposition. This is true in the smooth-wall case, but also away from the roughness sublayer (RSL) in a rough-wall flow.

Since the time-averaged fields are spatially inhomogeneous in the RSL and the spatial averages do not commute with spatial derivatives, applying the triple decomposition to transport equations yields form-induced (FI) terms, in addition to the regular, nonform-induced (NFI), ones. The FI terms represent the direct impact of the roughness on the flow; they vanish in a smooth-wall case. The NFI terms, which would also be present in a smooth-wall case, are formally unchanged; however, they can still be affected by the roughness indirectly [47].

## III. RESULTS

### A. Turbulent Prandtl number

In RANS solutions, or in any method in which averaging is applied, the turbulent stresses and fluxes need to be modeled. A variety of models have been devised to approximate them; the simplest techniques are based on the Boussinesq approximation, which relates the Reynolds stresses and scalar fluxes to the gradients of velocity and scalar concentration (or temperature) through an eddy viscosity  $\nu_T$  and an eddy diffusivity  $\alpha_T$ :

$$-\langle \overline{u'_i u'_j} \rangle_s + \frac{2\delta_{ij}}{3} \mathcal{K} = 2\nu_T \langle \overline{S}_{ij} \rangle_s, \quad -\langle \overline{\theta' u'_k} \rangle_s = \alpha_T \langle \overline{G}_k \rangle_s, \quad (8)$$

where  $\overline{S}_{ij}$  and  $\overline{G}_k$  are the time-averaged strain tensor and scalar gradient

$$S_{ij} = \frac{1}{2} \left( \frac{\partial \bar{u}_i}{\partial x_j} + \frac{\partial \bar{u}_j}{\partial x_i} \right), \quad G_k = \frac{\partial \bar{\theta}}{\partial x_k}. \quad (9)$$

The turbulent Prandtl number is defined as the ratio between  $\nu_T$  and  $\alpha_T$ , and can be calculated from experimental or numerical data by contracting Eq. (8) with  $\langle \overline{S}_{ij} \rangle_s$  [64] and  $\langle \overline{G}_k \rangle_s$  (see Appendix B

for details), resulting in

$$\text{Pr}_T = \frac{v_T}{\alpha_T} = \frac{\overline{u'v'}_s \frac{d\langle\bar{\theta}\rangle_s/dy}{\langle\bar{u}\rangle_s/dy}}{\langle\theta'v'\rangle_s \frac{d\langle\bar{u}\rangle_s/dy}{\langle\bar{u}\rangle_s/dy}}. \quad (10)$$

For a rough-wall case the governing equations for mean (time- and superficially averaged) momentum and scalar are [47]

$$-\langle\bar{\Pi}\rangle_s = \frac{d}{dy} \left[ v \frac{d\langle\bar{u}\rangle_s}{dy} - \langle u'v' \rangle_s - \langle \tilde{u}\tilde{v} \rangle_s \right] + f_p + f_v, \quad (11)$$

$$-\langle\bar{Q}\rangle_s = \frac{d}{dy} \left[ v \frac{d\langle\bar{\theta}\rangle_s}{dy} - \langle \theta'v' \rangle_s - \langle \tilde{\theta}\tilde{v} \rangle_s \right] + f_\alpha, \quad (12)$$

where  $\langle\bar{\Pi}\rangle_s$  and  $\langle\bar{Q}\rangle_s$  are the driving mean-pressure-gradient and scalar source-term, respectively. The terms in the square parenthesis on the right-hand side of both equations are the viscous, turbulent, and dispersive stress/flux terms, respectively. The dispersive terms arise from the the spatial inhomogeneity of the time-averaged velocity and scalar fields (also known as “wake fields”) due to the roughness; as such, they are nullified above the roughness.  $f_p$  and  $f_v$  are the form-induced pressure and viscous forces on the roughness elements, and  $f_\alpha$  accounts for the effect of heat transfer to the roughness elements [11,47]:

$$f_p = -\left\langle \frac{\partial \tilde{p}}{\partial x} \right\rangle_s, \quad f_v = \left\langle \frac{\partial}{\partial x_k} \left( v \frac{\partial \tilde{u}}{\partial x_k} \right) \right\rangle_s - 2v \frac{d\langle\bar{u}\rangle}{dy} \frac{d\phi}{dy} - v\langle\bar{u}\rangle \frac{d^2\phi}{dy^2}, \quad (13)$$

and

$$f_\alpha = \left\langle \frac{\partial}{\partial x_k} \left( \alpha \frac{\partial \tilde{\theta}}{\partial x_k} \right) \right\rangle_s - 2\alpha \frac{d\langle\bar{\theta}\rangle}{dy} \frac{d\phi}{dy} - \alpha\langle\bar{\theta}\rangle \frac{d^2\phi}{dy^2}. \quad (14)$$

A dispersive equivalent of the turbulent Prandtl number can be derived in a similar way as

$$\tilde{\text{Pr}}_T = \frac{\tilde{v}_T}{\tilde{\alpha}_T} = \frac{\langle \tilde{u}\tilde{v} \rangle_s \frac{d\langle\bar{\theta}\rangle_s/dy}{\langle \tilde{u}\tilde{v} \rangle_s \frac{d\langle\bar{u}\rangle_s/dy}{\langle \tilde{u}\tilde{v} \rangle_s}}}{\langle \tilde{\theta}\tilde{v} \rangle_s \frac{d\langle\bar{u}\rangle_s/dy}{\langle \tilde{u}\tilde{v} \rangle_s}}. \quad (15)$$

Alternatively, one can combine the stochastic and dispersive terms to derive an “effective” Prandtl number  $\text{Pr}_{T,\text{eff}}$  [33]:

$$\text{Pr}_{T,\text{eff}} = \frac{v_T + \tilde{v}_T}{\alpha_T + \tilde{\alpha}_T} = \frac{\langle u'v' + \tilde{u}\tilde{v} \rangle_s \frac{d\langle\bar{\theta}\rangle_s/dy}{\langle u'v' + \tilde{u}\tilde{v} \rangle_s \frac{d\langle\bar{u}\rangle_s/dy}{\langle u'v' + \tilde{u}\tilde{v} \rangle_s}}}{\langle \theta'v' + \tilde{\theta}\tilde{v} \rangle_s \frac{d\langle\bar{u}\rangle_s/dy}{\langle \theta'v' + \tilde{\theta}\tilde{v} \rangle_s}}. \quad (16)$$

This definition avoids the ill-conditioning of  $\tilde{\text{Pr}}_T$ , due to the fact that the dispersive stresses vanish a short distance above the roughness crest, and both denominator and numerator of Eq. (15) are small, resulting in a division of small numbers.

Figure 3 shows the turbulent Prandtl number  $\text{Pr}_T$  and the effective one,  $\text{Pr}_{T,\text{eff}}$ , for the smooth- and rough-wall cases. Since some of the reference data use  $\text{Pr} = 1$  and others  $\text{Pr} = 0.71$ , both values are shown in the figures; their behavior is, however, very similar. It is important to note that there is some variability in the scalar boundary-conditions between the studies: Some used constant internal heat-source (uniform forcing) based on Ref. [26], others used various implementations of a constant wall heat-flux. For example, Antonia *et al.* [19] used a strictly constant wall-flux by adding a spatially nonuniform source term [36,67] while Pirozzoli *et al.* [27] applied a running average to determine the mean wall-flux, allowing for 1% variation with respect to the imposed mean value. The approach by Antonia *et al.* [19] is almost identical to the one used here, which is reflected in the excellent agreement for  $\text{Pr} = 0.71$  (the only case studied). Considering the scatter of the reference data, probably due to the difference in the boundary-condition implementation and physical configuration, the present calculation can be considered in agreement with the other



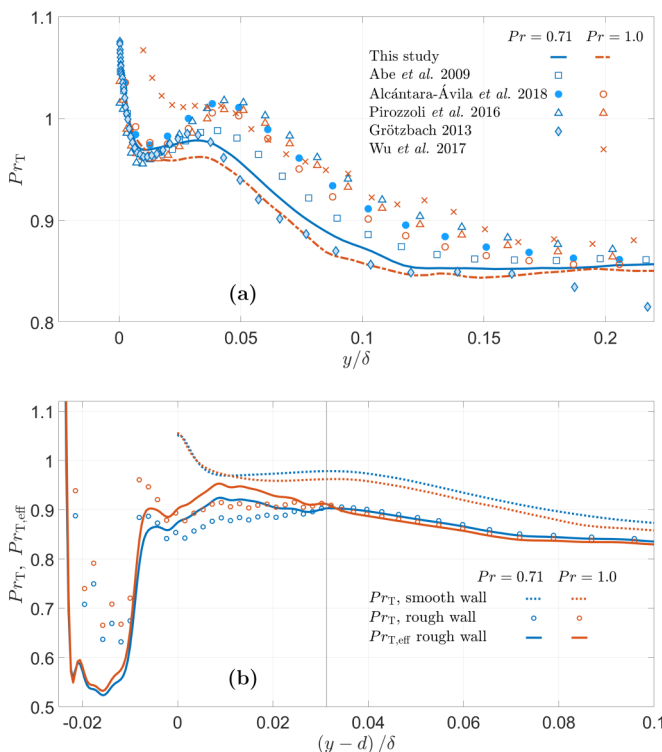


FIG. 3. Near-wall distribution of the Turbulent Prandtl Number  $Pr_T$  and effective Prandtl Number  $Pr_{T,eff}$  in (a) smooth-wall and (b) rough-wall cases, for  $Pr = 0.71$  (blue) and  $Pr = 1.0$  (orange). Studies cited in panel (a): [19,20,27,65,66].

studies. While a constant value  $Pr_T \approx 0.9$  is often assumed, the wall-normal variation of  $Pr_T$  is not negligible, starting from a value of 1.05 at the (smooth) wall and decreasing to 0.7 at the centreline.

In Fig. 3(b), we consider both  $Pr_T$  and  $Pr_{T,eff}$  for the rough-wall case and compare it with the smooth-wall behavior. As would be expected, both  $Pr_T$  and  $Pr_{T,eff}$  collapse with the smooth-wall equivalent above  $(y-d)/\delta \approx 0.15$ , a value four times larger than the roughness height, consistent with Townsend's similarity. Inside the RSL, for  $(y-d)/\delta \geq 0 \leq 0.04$ , both  $Pr_T$  and  $Pr_{T,eff}$  remain much closer to the value of 0.9 usually assumed in most models, and remain within a narrower range, compared to the smooth-wall case. Below the virtual wall however, both  $Pr_T$  and  $Pr_{T,eff}$  change drastically and increase monotonically approaching the base of the roughness,  $(y-d)/\delta \leq -0.02$ . Note that this region is usually outside the computational domain if the roughness is not directly resolved. The two different  $Pr$  cases show similar behavior, but with a shift.

Note that  $Pr_T$  and  $Pr_{T,eff}$ , inside the RSL are lower than  $Pr_T$  of the smooth case, in contrast to the results of Kuwata [33]; however, the steep increase of  $Pr_T$  and  $Pr_{T,eff}$  at the very bottom of the roughness (reaching much higher values than 1.0) is consistent with their result.

## B. Timescale ratio

The ratio between the integral timescale of the turbulent scalar fluctuation ( $\tau_\theta = \mathcal{K}_\theta/\varepsilon_\theta$ ) and that of the velocity fluctuation ( $\tau_k = \mathcal{K}/\varepsilon$ ), known as the timescale ratio  $\mathcal{R} = \tau_\theta/\tau_k$ , is another important quantity used heavily in modeling scalar transport, combustion, and simplified heat-transfer calculations [35]. It is central to modeling quantities such as the scalar variance dissipation  $\varepsilon_\theta$  in algebraic models and simplified analytic calculations [35,39,50]. In particular, the simplest algebraic

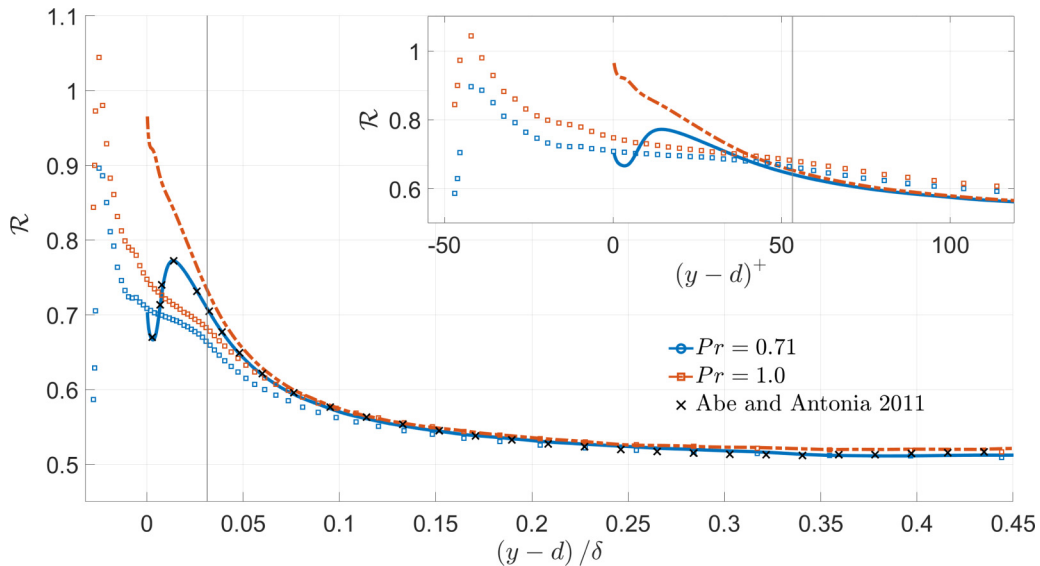


FIG. 4. Ratio of integral timescales  $\mathcal{R} = \tau_\theta/\tau$ . Lines: smooth-wall case; markers: rough-wall case. Inset is zoomed at the region around  $(y-d)^+ = 0$ .

model for  $\varepsilon_\theta$  uses the definition of  $\mathcal{R}$  to yield

$$\varepsilon_\theta = \mathcal{R}^{-1} \frac{\mathcal{K}_\theta}{\mathcal{K}} \varepsilon, \quad (17)$$

with  $\mathcal{R}$  being prescribed as constant or by some power law. It is often assumed in practical applications that  $\mathcal{R}$  is constant, and approximately equal to 0.5, which holds well away from the wall (note that in combustion,  $\mathcal{R}$  is usually defined as the inverse,  $\tau_k/\tau_\theta$ , and assumed to be approximately equal to 2.0).

Beguier *et al.* [35] concluded that  $\mathcal{R} \approx 0.5$  in local equilibrium. While indeed  $\mathcal{R} \approx 0.5$  holds well away from a solid boundary in many cases, Kawamura *et al.* [36] showed analytically, for a smooth-wall channel, that the timescale ratio  $\mathcal{R}$  tends to  $Pr$  as the wall is approached, independent of the Reynolds number. The smooth-wall results in Fig. 4, which match well those of Refs. [19,68], show a different behavior based on  $Pr$ . While  $Pr = 1.0$  shows a monotonic trend,  $Pr = 0.71$  has both local minima and maxima near the wall. The difference stems from the different thickness of the scalar diffusive-sublayer compared to that of the momentum: for  $Pr = 1.0$  both viscous and diffusive sublayers are of similar thickness; however for  $Pr = 0.71$  the scalar diffusive sublayer is thicker, resulting in the decrease of the scalar fluctuations further from the wall. Note that this near-wall behavior of  $\mathcal{R}$  was not reflected in  $Pr_T$  since  $\mathcal{R}$  only depends on the turbulent quantities while  $Pr_T$  also depends on viscous/diffusive terms; the viscous/diffusive terms increase near the wall to the same extent that the turbulent terms reduce, causing the different near-wall behavior between  $\mathcal{R}$  and  $Pr_T$  [36,68]. As shown in Fig. 4, this is not the case for a rough-wall: from the crest to the virtual wall  $\mathcal{R} < Pr$ , but increases monotonically and rapidly to larger values at the base of the roughness. The near-wall dependence on  $Pr$  still exists, but is considerably reduced compared with the smooth-wall case. This is likely due to the fact that roughness allows the turbulent motions to penetrate deep into the RSL, prevents the formation of a thick diffusive sublayer and removes the buffer layer [47,62]. Thus, the RSL is dominated by turbulence, which has little to no impact from the molecular diffusivity. However, the effect of  $Pr$  is not completely eliminated since there is still a thin diffusive layer that follows the geometry [32,47], maintaining some of the effect of  $Pr$ .

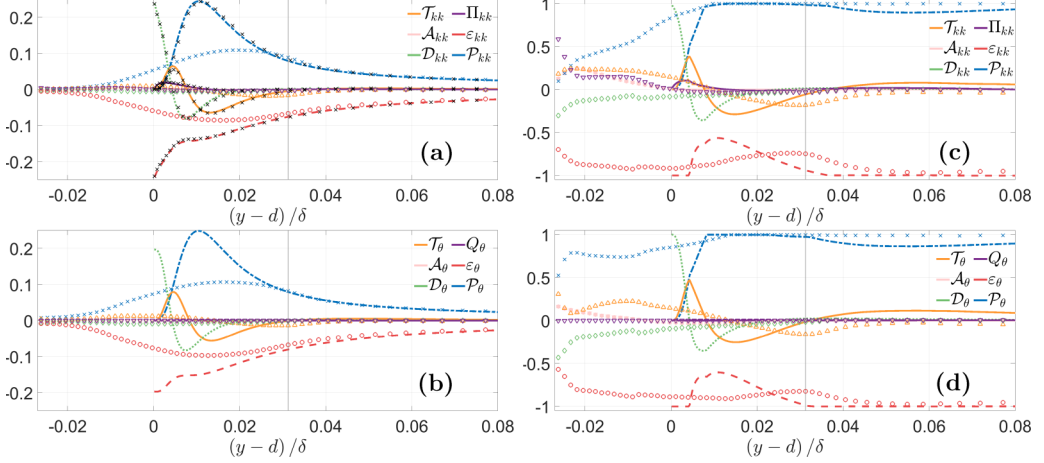


FIG. 5. Budgets of (a) TKE and (b) scalar variance with  $\text{Pr} = 1.0$ , normalized by wall units ( $u_\tau$ ,  $\theta_\tau$ , and  $\nu$ ); panels (c) and (d) show the relative contribution of each term in the corresponding budget. Lines used for smooth-wall case and markers for rough-wall.  $\times$ : DNS from Abe *et al.* [67]. The vertical line marks the roughness crest.

Townsend's similarity hypothesis was shown to extend and hold for many different turbulent quantities [31,32,47,54,61,62,69]. As could be expected, it also holds for both timescales (not shown here), and as a result for their ratio  $\mathcal{R}$ : both smooth- and rough-wall timescales collapse on the smooth-wall case rather quickly above the RSL.

### C. Turbulent kinetic energy and scalar-variance budgets

Hantsis and Piomelli [47] compared the budgets of the scalar variance  $\mathcal{K}_\theta$  and the streamwise Reynolds stress  $\langle \overline{u'u'} \rangle_s$ , including the effects of roughness on the budgets. Much of the analogy between momentum and scalar transport stems from the streamwise component, which dominates momentum transport and the TKE  $\mathcal{K}$  budget. The model is the equation of  $\mathcal{K}_\theta$ ; however, it is developed in analogy to that of  $\mathcal{K}$ , which has some differences from that of the streamwise Reynolds stress. For this reason we will briefly discuss the TKE budget, focusing on modeling issues.

The budgets of the TKE  $\mathcal{K}$  and scalar variance  $\mathcal{K}_\theta$  in a plane channel are

$$0 = \mathcal{P}_{kk} + \mathcal{A}_{kk} + \mathcal{T}_{kk} + \mathcal{D}_{kk} - \varepsilon_{kk} + \Pi_{kk}, \quad (18)$$

$$0 = \mathcal{P}_\theta + \mathcal{A}_\theta + \mathcal{T}_\theta + \mathcal{D}_\theta - \varepsilon_\theta + Q_\theta, \quad (19)$$

where the terms on the right-hand side of these equations are the production  $\mathcal{P}$ , mean (or wake) transport  $\mathcal{A}$ , turbulent transport  $\mathcal{T}$ , diffusion  $\mathcal{D}$  and dissipation  $\varepsilon$ . In addition, Eq. (18) contains the pressure-work term  $\Pi_{kk}$  and Eq. (19) contains the source term  $Q_\theta$ . For the explicit expressions of the terms and additional details see Ref. [47].

Figures 5(a) and 5(b) show the budgets of the  $\mathcal{K}$  and  $\mathcal{K}_\theta$ , respectively, as well as the relative contributions of each term in Figs. 5(c) and 5(d). The relative contribution  $g_{i,\text{rel}}$  of a term  $g_i$  is calculated as  $g_{i,\text{rel}} = g_i / (2 \sum_k |g_k|)$ ; with this definition the sum of all relative contributions is zero; if two terms dominate, each has a value of  $\pm 1.0$ .

Hantsis and Piomelli [47] observed that the scalar form-induced (FI) production  $\mathcal{P}_\theta^{\text{fi}}$ , being the dominant source term in the RSL, is more significant than the corresponding FI production component of the streamwise velocity fluctuation  $\langle \overline{u'u'} \rangle$ ,  $\mathcal{P}_{11}^{\text{fi}}$ . This difference is mainly due to the dissimilarity between the wake fields of  $\theta$  and  $\tilde{u}$ , as well as the magnitude of the different roughness

functions, resulting in  $\langle \bar{\theta} \rangle^+ > \langle \bar{u} \rangle^+$  within the RSL, for all the Pr examined. In terms of  $\mathcal{K}$ , the FI production  $\mathcal{P}_{kk}^{fi}$  is (half) the sum of contributions from the three fluctuating velocity components ( $k = 1, 2, 3$ ). Since both  $\mathcal{P}_{22}^{fi}$  and  $\mathcal{P}_{33}^{fi}$  are significantly smaller than  $\mathcal{P}_{11}^{fi}$ ,  $\mathcal{P}_{kk}^{fi}$  effectively behaves like  $\mathcal{P}_{11}^{fi}$  and therefore is smaller than the  $\mathcal{K}_\theta$  comparable term,  $\mathcal{P}_\theta^{fi}$ .

For  $\langle \overline{u'u'} \rangle_s$  the contribution of the pressure-work term ( $\Pi_{11}$ ) was significant [47] and a key difference from the scalar variance budget. For the  $\mathcal{K}$  budget, however, the pressure-work term contribution ( $\Pi_{kk}$ ) is negligible for  $y - d \geq 0$ , as the pressure fluctuations mainly redistribute the energy between the normal stress components. Thus, the budget of  $\mathcal{K}_\theta$  is more similar to that of the  $\mathcal{K}$  compared with  $\langle \overline{u'u'} \rangle_s$ . Deeper in the roughness sublayer, where  $\Pi_{kk}$  becomes more important [Fig. 5(c)] all the TKE budget terms, as well as  $\mathcal{K}$  itself, become very small.

The relative contributions shows that in both  $\mathcal{K}$  and  $\mathcal{K}_\theta$ , the overall rough-wall behavior can be adequately approximated by  $\mathcal{P} \approx \varepsilon$ , all other terms being negligible; this was not the case for  $\langle \overline{u'u'} \rangle_s$ . This approximation is valid all the way to the virtual wall at  $y - d = 0$ , which would be the boundary when the roughness geometry is substituted by a model, as is the case in RANS. In fact, for  $\mathcal{K}_\theta$  this approximation is valid all the way to the very bottom of the roughness sublayer. Note that here  $\mathcal{P}$  includes both shear and FI production. This simple  $\mathcal{P} \approx \varepsilon$  behavior is very useful for roughness modeling. In particular, when double-averaged quantities are used to describe the macroscopic behavior due to roughness (such as the DANS methodology), the shear and FI components of  $\mathcal{P}$  can be modeled independently.

#### D. Dissipation budget

Many turbulence models employ a transport equation for the scalar dissipation-rate  $\varepsilon_\theta$ . Unlike the TKE or scalar-variance equations, the exact dissipation transport equation is rarely used for modeling [17], and all the budget terms are derived from phenomenological considerations. The double-averaged dissipation transport equation can be written as

$$\begin{aligned}
 0 = & \underbrace{-2\alpha \left\langle \left( \overline{u'_i \frac{\partial \theta'}{\partial x_k}} \right) \frac{\partial^2 \bar{\theta}}{\partial x_i \partial x_k} \right\rangle_s}_{\mathcal{P}_{\varepsilon\theta}^G} - \underbrace{2\alpha \left\langle \left( \overline{\frac{\partial u'_i}{\partial x_k} \frac{\partial \theta'}{\partial x_k}} \right) \frac{\partial \bar{\theta}}{\partial x_i} \right\rangle_s}_{\mathcal{P}_{\varepsilon\theta}^{\text{MS}}} - \underbrace{2\alpha \left\langle \left( \overline{\frac{\partial \theta'}{\partial x_k} \frac{\partial \theta'}{\partial x_i}} \right) \frac{\partial \bar{u}_i}{\partial x_k} \right\rangle_s}_{\mathcal{P}_{\varepsilon\theta}^{\text{MV}}} - \underbrace{\alpha \left\langle \overline{\frac{\partial \theta'}{\partial x_k} \frac{\partial \theta'}{\partial x_i} \frac{\partial u'_i}{\partial x_k}} \right\rangle_s}_{\mathcal{P}_{\varepsilon\theta}^T} \\
 & - \underbrace{\left\langle \frac{\partial}{\partial x_i} \left( \overline{u'_i \varepsilon_\theta} \right) \right\rangle_s}_{\mathcal{T}_{\varepsilon\theta}} - \underbrace{\left\langle \frac{\partial}{\partial x_i} \left( \overline{\bar{u}_i \varepsilon_\theta} \right) \right\rangle_s}_{\mathcal{A}_{\varepsilon\theta}} + \underbrace{\alpha \left\langle \frac{\partial^2 \bar{\varepsilon}_\theta}{\partial x_i \partial x_i} \right\rangle_s}_{\mathcal{D}_{\varepsilon\theta}} - \underbrace{2\alpha^2 \left\langle \left( \overline{\frac{\partial^2 \theta'}{\partial x_i \partial x_k} \frac{\partial^2 \theta'}{\partial x_i \partial x_k}} \right) \right\rangle_s}_{\varepsilon_{\varepsilon\theta}} + \underbrace{2\alpha \left\langle \frac{d(T_w)}{dx} \overline{\frac{\partial \theta'}{\partial x_k} \frac{\partial u'_i}{\partial x_k}} \right\rangle_s}_{Q_{\varepsilon\theta}}, \tag{20}
 \end{aligned}$$

where the terms are: (1) gradient production  $\mathcal{P}_{\varepsilon\theta}^G$ , (2) mean scalar gradient production  $\mathcal{P}_{\varepsilon\theta}^{\text{MS}}$ , (3) mean velocity-gradient production  $\mathcal{P}_{\varepsilon\theta}^{\text{MV}}$ , (4) turbulent production  $\mathcal{P}_{\varepsilon\theta}^T$  (stretching of the scalar field by turbulent strain), (5) turbulent transport  $\mathcal{T}_{\varepsilon\theta}$ , (6) mean transport  $\mathcal{A}_{\varepsilon\theta}$ , (7) molecular diffusion  $\mathcal{D}_{\varepsilon\theta}$ , (8) molecular dissipation  $\varepsilon_{\varepsilon\theta}$ , and (9) source term contribution  $Q_{\varepsilon\theta}$  (due to wall scalar flux in our case, but can be due to reactions and other sources).

The scalar-dissipation budget terms for smooth-wall and rough-wall cases and Pr = 0.71 are shown in Fig. 6. Figure 6(a) shows the smooth-wall case and the data from Abe *et al.* [18], in inner scaling. Both smooth- and rough-wall cases are shown in Fig. 6(b). The terms are normalized using  $u_\tau$ ,  $\theta_\tau$ ,  $\nu$ , and Pr. The vertical line in Fig. 6(b) identifies the roughness crest. For the smooth case (lines), good agreement with Ref. [18] (black markers) is found both in terms of magnitude and behavior. The largest differences in the production and dissipation terms is less than 6%. These differences may be due to the slight difference in the scalar boundary-conditions between this work and Abe *et al.* [18]; altogether, the results trends are consistent with Refs. [18,49] and show the same key features: the near-wall dominance of three production (of scalar dissipation) terms  $\mathcal{P}_{\varepsilon\theta}^T$ ,

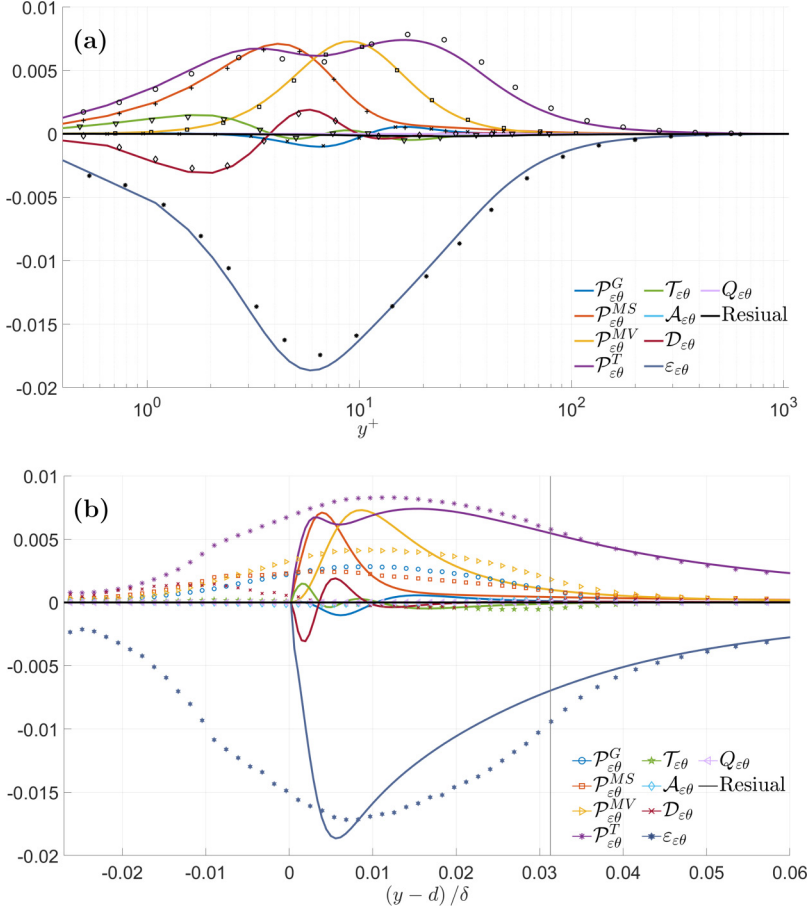


FIG. 6. Scalar dissipation budget for  $Pr = 0.71$ : (a) smooth-wall only, black markers are reference data from Abe *et al.* [18]; (b) smooth-wall (lines) and rough-wall (markers, corresponding colors). All budget terms are normalized by wall units using  $u_\tau$ ,  $\theta_\tau$ ,  $\nu$ , and  $\alpha$ . The vertical line marks the roughness crest.

$\mathcal{P}_{\varepsilon\theta}^{MS}$ , and  $\mathcal{P}_{\varepsilon\theta}^{MV}$  along with the dissipation (of dissipation) term  $\varepsilon_\theta$ , while away from the wall only  $\mathcal{P}_{\varepsilon\theta}^T$  and  $\varepsilon_\theta$  remain dominant with diminishing in magnitude further from the wall.

In Fig. 6(b) we compare the smooth-wall case (lines) with the rough-wall one (markers with matching color). Both turbulent production of scalar dissipation  $\mathcal{P}_{\varepsilon\theta}^T$  and dissipation of scalar dissipation  $\varepsilon_{\varepsilon\theta}$  are dominant away from the wall, consistent with other studies. These two terms remain the most significant inside the RSL, making them the dominant terms throughout the entire domain.  $\mathcal{P}_{\varepsilon\theta}^T$  has the same (normalized) magnitude as the smooth wall while  $\mathcal{P}_{\varepsilon\theta}^{MS}$  and  $\mathcal{P}_{\varepsilon\theta}^{MV}$ , which are significant in the smooth-wall case, decrease significantly, making  $\mathcal{P}_{\varepsilon\theta}^T$  the most dominant source term throughout the entire domain. In the smooth case, however, they decrease as the wall is approached. However, the remaining production (of dissipation) terms are not negligible in the rough case;  $\mathcal{P}_{\varepsilon\theta}^{MV}$  is approximately equal to half of  $\mathcal{P}_{\varepsilon\theta}^T$  while  $\mathcal{P}_{\varepsilon\theta}^G$  and  $\mathcal{P}_{\varepsilon\theta}^{MS}$  are roughly one-third of  $\mathcal{P}_{\varepsilon\theta}^T$  each. Together,  $\mathcal{P}_{\varepsilon\theta}^G$ ,  $\mathcal{P}_{\varepsilon\theta}^{MV}$ , and  $\mathcal{P}_{\varepsilon\theta}^{MS}$  give about the same contribution as  $\mathcal{P}_{\varepsilon\theta}^T$ . The increase of the magnitude of  $\mathcal{P}_{\varepsilon\theta}^G$  compared to the smooth-wall case is directly associated with the roughness geometry, which forces a larger curvature of the  $\bar{\theta}$  isosurfaces, which follow the geometry closely; this will be further discussed later.

A similar trend,  $\mathcal{P}_{\varepsilon\theta}^T$  becoming more dominant over the other production terms, was also observed by Ref. [52] in a smooth-wall channel, when  $\text{Pe}_\tau = \text{Re}_\tau \text{Pr}$  was increased; the effect of increasing  $\text{Pr}$  was more significant than an equivalent increase in  $\text{Re}_\tau$  (resulting in the same  $\text{Pe}$ ). While the increase of  $\text{Pe}$  for the smooth-wall case had a very similar trend to the addition of roughness (without changing  $\text{Pe}$ ), the increase was not as marked as that due to the roughness. Abe *et al.* [18] and [52] showed that the  $\varepsilon_\theta$  budget terms collapse away from the (smooth) wall for the different values of  $\text{Pe}$ . This is consistent with Townsend's similarity and the fact that away from the (smooth) wall the flow field is dominated by turbulent motions. This is also true for the rough-wall case, as all the rough-wall terms collapse on the corresponding smooth-wall ones a few roughness-heights above the crest. When compared to the addition of roughness, increasing  $\text{Pe}$  provided a very similar trend to adding roughness. However, it does appear that adding roughness might have an effect equivalent to a significant increase of  $\text{Pe}$ .

The turbulent transport of scalar dissipation  $\mathcal{T}_{\varepsilon\theta}$  and the diffusion of scalar dissipation  $\mathcal{D}_{\varepsilon\theta}$  are insignificant for  $y - d > 0$  while for  $y - d \leq 0$  the diffusion term  $\mathcal{D}_{\varepsilon\theta}$  becomes comparable to  $\mathcal{P}_{\varepsilon\theta}^T$ , each of them balancing about half of  $\varepsilon_{\varepsilon\theta}$ . The mean transport  $\mathcal{A}_{\varepsilon\theta}$ , which was identically zero for the smooth-wall case, remains the smallest of the transport terms and can be neglected in the rough-wall case as well.

$\mathcal{P}_{\varepsilon\theta} \approx \varepsilon_{\varepsilon\theta}$  holds well from the virtual wall outward for the scalar dissipation budget, in a similar manner to the behavior of the  $\langle \overline{\theta'\theta'} \rangle_s$  budget. In the rough-wall case, the different budget terms, including those of  $\mathcal{K}_\theta$  and  $\varepsilon_\theta$ , tend to the same form, with a peak around  $(y - d)/\delta \approx 0.01$  followed by a similar simple increase or decrease for all the the other terms. Thus, it seems that in terms of the 1D statistics, roughness reducing the complexity of the near-wall in the smooth case, significantly simplifying the problem to a  $\mathcal{P} \approx \varepsilon$  type of equilibrium, which is more amenable to modeling.

Many of the terms in Eq. (20) have a form-induced (FI) and non form-induced (NFI) contributions. We consider the following terms:

$$\begin{aligned}\mathcal{P}_{\varepsilon\theta}^G &= \tilde{\mathcal{P}}_{\varepsilon\theta}^G - 2\alpha \left\langle v' \frac{\partial \theta'}{\partial y} \right\rangle_s \frac{d^2 \langle \bar{\theta} \rangle}{dy^2} \\ \mathcal{P}_{\varepsilon\theta}^{\text{MS}} &= \tilde{\mathcal{P}}_{\varepsilon\theta}^{\text{MS}} - 2\alpha \left\langle \frac{\partial v'}{\partial x_k} \frac{\partial \theta'}{\partial x_k} \right\rangle \frac{d \langle \bar{\theta} \rangle_s}{dy} \\ \mathcal{P}_{\varepsilon\theta}^{\text{MV}} &= \tilde{\mathcal{P}}_{\varepsilon\theta}^{\text{MV}} - 2\alpha \left\langle \frac{\partial \theta'}{\partial x} \frac{\partial \theta'}{\partial y} \right\rangle \frac{d \langle \bar{u} \rangle_s}{dy}\end{aligned}\quad (21)$$

where the FI term is denoted with a tilde (for more details, see Appendix A). The breakdown of these terms is shown in Fig. 7; the FI contributions are shown by dashed lines and the NFI contributions by dotted lines. The total is as shown in Fig. 6 and uses the same markers and colors.

As mentioned before, the gradient production-of-dissipation  $\mathcal{P}_{\varepsilon\theta}^G$  is more significant in the rough case than in the smooth case, as it depends strongly on the curvature of the of the isosurfaces of time-averaged scalar field  $\bar{\theta}$  via the 2<sup>nd</sup>-order spatial derivatives; the roughness geometry directly affects the curvature, since the mean scalar isosurfaces follow the roughness geometry closely without significant separation regions, a phenomenon discussed by Refs. [31,47], and shown in Fig. 8. Furthermore, Fig. 7, shows how the entire  $\mathcal{P}_{\varepsilon\theta}^G$  is due to the FI contribution  $\tilde{\mathcal{P}}_{\varepsilon\theta}^G$ . However, for  $\mathcal{P}_{\varepsilon\theta}^{\text{MS}}$  and  $\mathcal{P}_{\varepsilon\theta}^{\text{MV}}$ , the FI contributions are much less significant, suggesting that in these terms the effect of the geometry is mostly indirect. Overall, the total FI contribution of the three production terms is about the same as the NFI contribution.

To better understand the role of the FI and NFI contributions, we define a ‘‘local production’’  $\hat{\mathcal{P}}$ , a quantity whose superficial average is equal to a corresponding production term  $\mathcal{P}$ :

$$\langle \hat{\mathcal{P}} \rangle_s = \frac{1}{A_0} \int_{A_f} \hat{\mathcal{P}} dA = \mathcal{P}. \quad (22)$$



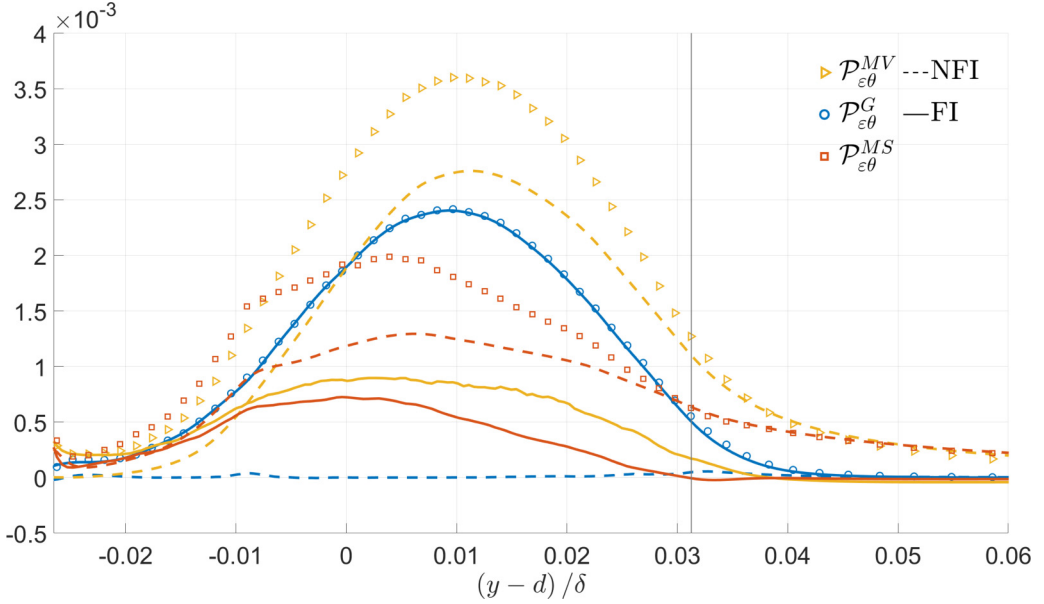


FIG. 7. Breakdown of the rough-wall production terms shown in Fig. 6. Markers: total contribution; ---- nonform-induced (NFI) part; — form-induced (FI) part. Normalization is the same as in Fig. 6.

The components  $\widehat{\mathcal{P}}_{\epsilon\theta}^G$ ,  $\widehat{\mathcal{P}}_{\epsilon\theta}^{MS}$ ,  $\widehat{\mathcal{P}}_{\epsilon\theta}^{MV}$ , and  $\widehat{\mathcal{P}}_{\epsilon\theta}^T$ , shown in Figs. 9(a)–9(d), would then be the expressions inside the spatial averaging operator  $(\bullet)_s$  of the corresponding production terms in Eq. (20). Note that these expressions contain both FI and NFI contributions.  $\widehat{\mathcal{P}}_{\epsilon\theta}^G$  is only significant near the roughness surface, in particular around the upstream side and over crests of the roughness elements, where the diffusive film of  $\bar{\theta}^+ < 5.0$  changes thickness rapidly or becomes distorted, causing the large gradients in  $\bar{\theta}$ .  $\widehat{\mathcal{P}}_{\epsilon\theta}^{MS}$  is most significant in the shear layers formed at the top of the crests, and in small, concentrated spots just ahead of the crests, where the FI contribution is lower. Both these terms do not extend far from the roughness;  $\widehat{\mathcal{P}}_{\epsilon\theta}^{MV}$  has very significant contributions right at the roughness surface, larger than those of  $\widehat{\mathcal{P}}_{\epsilon\theta}^G$  or  $\widehat{\mathcal{P}}_{\epsilon\theta}^{MS}$ ; however, some of these are negative and appreciably reduce the resulting FI contribution of  $\mathcal{P}_{\epsilon\theta}^{MS}$ . In the gaps between elements  $\widehat{\mathcal{P}}_{\epsilon\theta}^{MV}$  also has both positive and negative contributions. This term is significant further away from the roughness, compared with  $\widehat{\mathcal{P}}_{\epsilon\theta}^{MS}$ . Overall,  $\widehat{\mathcal{P}}_{\epsilon\theta}^{MV}$  is a dominant term locally; however, significant negative values reduce its averaged value,  $\mathcal{P}_{\epsilon\theta}^{MV}$ , which is roughly equal to  $\mathcal{P}_{\epsilon\theta}^{MS}$ . Finally,  $\widehat{\mathcal{P}}_{\epsilon\theta}^T$  is significant throughout the RSL, both near and between roughness elements and is the dominant term above the roughness. Since  $\mathcal{P}_{\epsilon\theta}^T$  does not depend directly on the mean scalar or velocity fields, it has no FI component. However, significant contributions to  $\widehat{\mathcal{P}}_{\epsilon\theta}^T$  occur due to the strong turbulent motions impinging on the upstream sides of the roughness elements [31,32] (where the diffusive  $\bar{\theta}^+ < 5$  film is thinner) and in the shear-layers that emanate from the roughness crests and extend downstream of them.

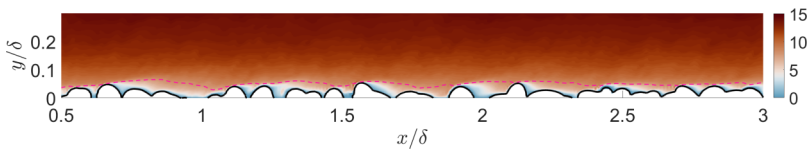


FIG. 8. Spatial distribution of  $\bar{\theta}^+$ . Blue region denotes where  $\bar{\theta}^+ < 5.0$ ; Dashed magenta line denotes the isocontour of  $\bar{u}^+ = 5$ .

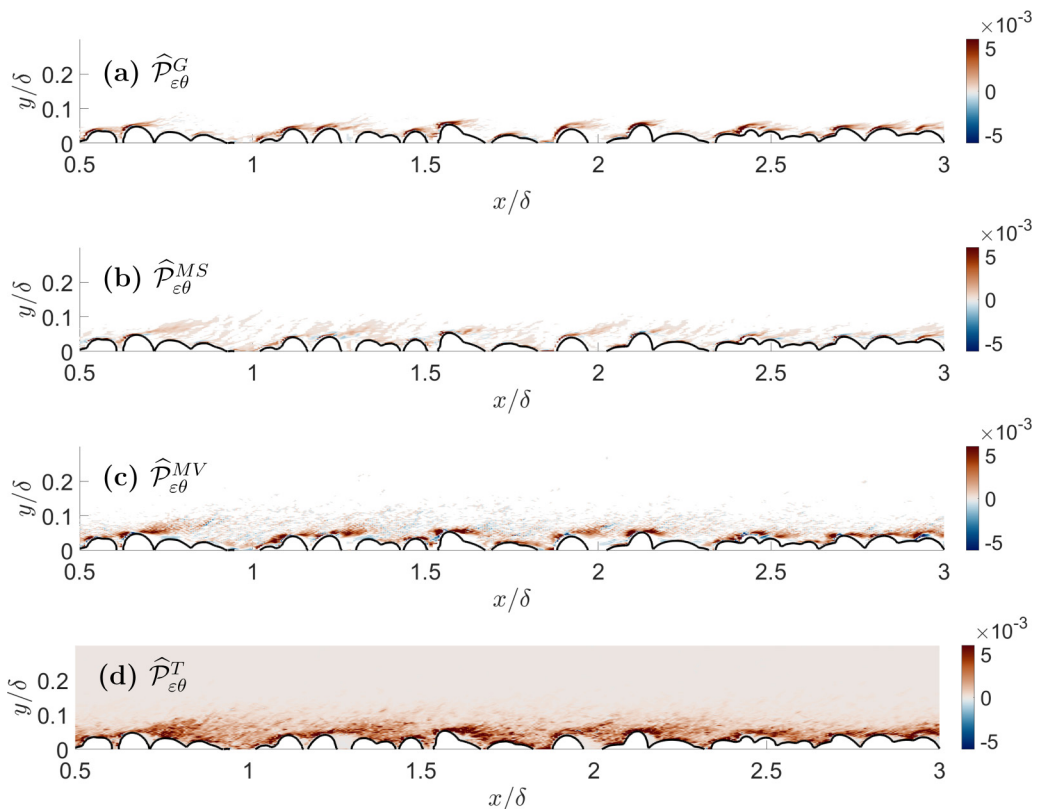


FIG. 9. Spatial distribution in  $XY$  plane of (a)  $\hat{\mathcal{P}}_{\varepsilon\theta}^G$ , (b)  $\hat{\mathcal{P}}_{\varepsilon\theta}^{MS}$ , (c)  $\hat{\mathcal{P}}_{\varepsilon\theta}^{MV}$ , and (d)  $\hat{\mathcal{P}}_{\varepsilon\theta}^T$ .

Since the leading production term,  $\mathcal{P}_{\varepsilon\theta}^T$ , has no FI component, altogether only a small part of the scalar dissipation generation is due to FI contributions; This is in contrast to the scalar variance  $\langle \theta'^2 \rangle_s$ , for which the generation in the RSL is dominated by the FI production term [47]. Note that the remaining terms in Eq. (20) either do not have a direct FI part or, if they have it, it is negligibly small.

### E. Analysis of the turbulent production-of-dissipation term

A better understanding of the turbulent production terms is necessary to gain further insight into the production (of scalar dissipation) process in view of the leading-order magnitude of these terms across the channel. As shown,  $\mathcal{P}_{\varepsilon\theta}^T$  is the dominant production in the rough-wall case and reproducing it correctly is a crucial part of any model that solves a transport equation for  $\varepsilon_\theta$ .  $\mathcal{P}_{\varepsilon\theta}^T$  has been studied both in cases without a solid boundary (such as homogeneous isotropic turbulence and homogeneous sheared turbulence [39,49–51,70–72]) and in smooth-wall bounded flows (such as channel flow [18,20]); however, the authors are not aware of any rough-wall analysis of this term.

$\mathcal{P}_{\varepsilon\theta}^T$  can be expressed in terms of the eigenvalues and eigenvectors of the fluctuating strain tensor  $s'_{ij}$ .  $\lambda_1 > \lambda_2 > \lambda_3$  are the eigenvalues, and  $\vec{\psi}^i$  ( $i = 1, 2, 3$ ) is the set of corresponding eigenvectors (i.e., the principal directions of strain):

$$\begin{aligned} \mathcal{P}_{\varepsilon\theta}^T &= -2 \left\langle \alpha \frac{\partial \theta'}{\partial x_i} \frac{\partial \theta'}{\partial x_j} 2s'_{ij} \right\rangle_s \\ &= -2 \overline{\langle \alpha |\nabla \theta'|^2 (\lambda_1 \cos^2 \beta_1 + \lambda_2 \cos^2 \beta_2 + \lambda_3 \cos^2 \beta_3) \rangle_s}, \end{aligned} \quad (23)$$

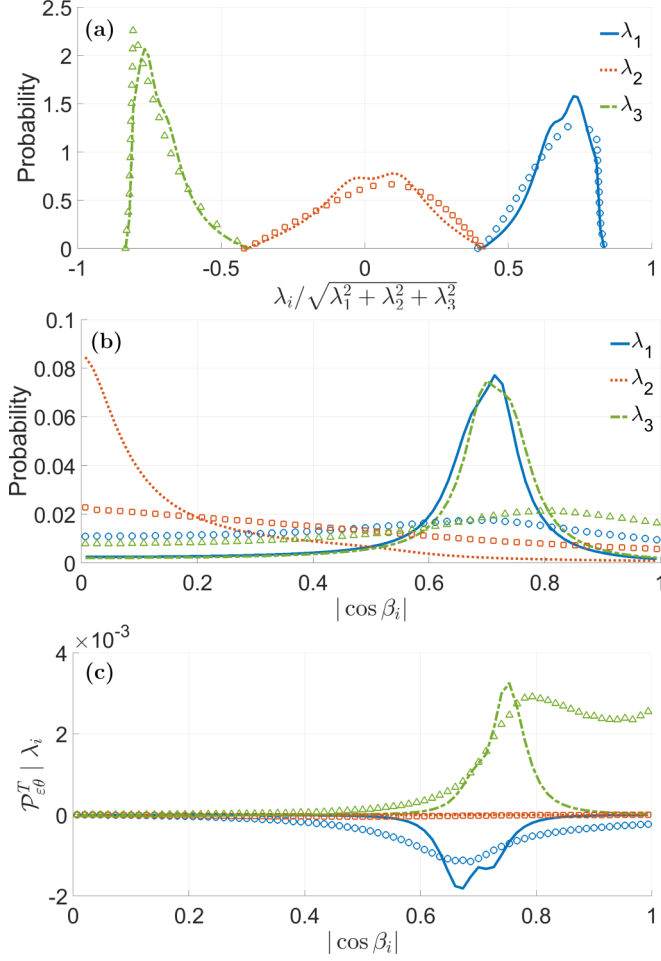


FIG. 10. Distribution and orientation of principal stresses and contribution to turbulent production  $\mathcal{P}_{\varepsilon\theta}^T$ . (a) Eigenvalue probability distribution; (b) probability of the angle cosine between the principal-stress directions  $\vec{\psi}^i$  and the fluctuating scalar gradient  $\nabla\theta'$ ; (c) contributions to  $\mathcal{P}_{\varepsilon\theta}^T$  conditioned on the eigenvalue  $\lambda_i$  and alignment angle  $\beta_i$ . Lines: smooth-wall case; markers: rough-wall case. Distribution taken at  $(y-d)^+ = 5$  and for  $\text{Pr} = 1.0$ .  $\mathcal{P}_{\varepsilon\theta}^T$  normalization is the same as in Fig. 6.

where  $\beta_i$  are the angles formed between the gradient of the fluctuating scalar  $\nabla\theta' = \partial\theta'/\partial x_k$  and the eigenvectors  $\vec{\psi}^i$ :

$$\cos \beta_i = \frac{\nabla\theta' \cdot \vec{\psi}^i}{|\nabla\theta'| |\vec{\psi}^i|}. \quad (24)$$

Equation (23) shows that positive contributions to  $\mathcal{P}_{\varepsilon\theta}^T$  can only come from compressive stresses (for which  $\lambda < 0$ ) while extensional stresses can only decrease  $\mathcal{P}_{\varepsilon\theta}^T$ . Additionally,  $\mathcal{P}_{\varepsilon\theta}^T$  is strongly dependent on the alignment between the direction of the principal stresses ( $\vec{\psi}_i$ ) with the direction of the scalar gradient, through  $\cos^2 \beta_i$  [18].

Figure 10(a) shows the probability distributions of the principal strain eigenvalues  $\lambda_i$  normalized by the total stress magnitude, taken at the plane  $(y-d)^+ = 5$ , which is close to the wall in the smooth-wall case and well within the RSL in the rough-wall case. The distributions, for

both smooth- and rough-wall geometries, show significant resemblance to those of Nomura and Elghobashi [49] in homogeneous sheared turbulence, confirming that the compressive principal stress  $\lambda_3$  tends to be larger than the extensional one  $\lambda_1$ , while  $\lambda_2$  is only slightly biased toward extensional stresses. Wu *et al.* [73] (who studied rotating channel flows), observed that in the RSL, turbulence is near the axisymmetric compression line, rather than axisymmetric expansion (for smooth-wall), suggesting increased dominance of compression at the wall. Overall, we see that while the roughness tends to increase the probability of stronger  $\lambda_3$  and somewhat decreases  $\lambda_1$ , these difference are not significant.

The probability of alignment between the principal strain directions and the scalar gradient is shown in Fig. 10(b) at the same location. In the smooth-wall case, both  $\vec{\psi}^1$  and  $\vec{\psi}^2$  tend to form a  $45^\circ$  angle with  $\nabla\theta'$ , while  $\vec{\psi}^3$  tends to be perpendicular to it, matching the results of Ref. [18] closely. For the rough-wall case, the distribution is significantly more uniform, with  $\vec{\psi}^3$  showing a higher probability of alignment ( $0.7 < |\cos \beta_3|$ ) compared with  $\vec{\psi}^1$  and  $\vec{\psi}^2$ .

Finally, Fig. 10(c) presents the contributions to  $\mathcal{P}_{\varepsilon\theta}^T$  from each of the principal strain components  $\lambda_i$  and as function of the alignment angle  $\beta_i$ . For both smooth- and rough-wall cases, the intermediate eigenvalue  $\lambda_2$  has negligible contribution, due to positive and negative values canceling each other and to poor alignment with  $\nabla\theta'$ . Thus,  $\mathcal{P}_{\varepsilon\theta}^T$  is effectively due to the difference between the contributions of the main extensional and compressive strain components.

The  $\mathcal{P}_{\varepsilon\theta}^T$  contribution due to the extensional eigenvalue  $\lambda_1$  behaves similarly in smooth-and rough-wall cases; for the smooth-wall the contribution is limited to a narrower range of angles around  $\beta_1 \approx 45^\circ$ , while for the rough case it is spread over a wider range. The main difference in  $\mathcal{P}_{\varepsilon\theta}^T$  between the smooth- and rough-wall cases is due to the compressive component,  $\lambda_3$ , and is most evident when the alignment between  $\vec{\psi}^3$  and  $\nabla\theta'$  is very good. Since the distribution of the eigenvalues  $\lambda_i$  is similar between the smooth- and rough-wall cases, this suggests that the increased alignment, due to roughness, holds the key to the different behavior between the two cases. These results are valuable for extending PDF methods [74,75] to the a rough-wall case.

#### IV. CONCLUSIONS AND DISCUSSION

A direct numerical simulation (DNS) of the transport of a passive scalar in a fully developed turbulent channel with rough walls was performed; the results are used to understand how to incorporate the effects of roughness into turbulence models of passive scalars. While several rough-wall corrections have been developed for momentum transport turbulence models in the context of for the Reynolds-averaged Navier-Stokes (RANS) equations, analogous modifications for the modeling of passive scalars are less advanced. Formulating rough-wall corrections to existing scalar models requires the knowledge of the behavior of the two main transported quantities (scalar variance and dissipation), as well as the key quantities used in these models, namely, the turbulent Prandtl number and timescale ratio. Our investigation aims to provide modelers with the information needed to incorporate the effects of roughness effects into existing scalar closure models and develop new ones.

The turbulent Prandtl number  $\text{Pr}_T$  is extensively used both in simplified calculations and turbulence models of scalar transport, and is often taken as a constant,  $\text{Pr}_T \approx 0.8\text{--}0.9$ , despite the fact that it is known to depart from that range near a smooth wall [16]. For the rough-wall case,  $\text{Pr}_T$  is indeed almost constant from the roughness centroid up to the crest  $\text{Pr}_T \approx 0.9$ , in line with the assumptions commonly used in modeling. Its rough-wall value is smaller than the smooth-wall one above the centroid. Below the centroid it changes rapidly, ranging from about 0.6 and up to 4.0 at the very base of the roughness. This region, however, is usually neglected in turbulence models, in which the virtual wall is taken to be the centroid location. Various studies reported different near-wall behavior of  $\text{Pr}_T$  [32,33,76], suggesting possible dependence on boundary conditions, roughness regime, type of roughness (in particular d-type versus k-type in transitional roughness) or other factors; further studies are required to determine whether the present results can be generalized to other conditions.

Away from the wall, Townsend's similarity hypothesis holds; the smooth- and rough-wall cases curves collapse.

Since additional dispersive terms exist in both the stress and scalar flux, they can be merged with the corresponding turbulent stresses and fluxes to form an effective turbulent Prandtl number,  $\text{Pr}_{\text{T,eff}}$ .  $\text{Pr}_{\text{T,eff}}$  collapsed on  $\text{Pr}_{\text{T}}$  above the roughness and has an overall behavior similar to  $\text{Pr}_{\text{T}}$  inside the roughness. Some variation can be seen below the centroid of the roughness, however it is only significant at the very base of the roughness and  $\text{Pr}_{\text{T,eff}}$  is slightly better behaved. Although only a limited range of  $\text{Pr}$  and one type of roughness were examined, these results suggest that  $\text{Pr}_{\text{T}}$  and  $\text{Pr}_{\text{T,eff}}$  can be used interchangeably, and the approximation  $\text{Pr}_{\text{T}} \approx \text{Pr}_{\text{T,eff}} \approx 0.9$  may be accurate enough (with relative error of 6% for both  $\text{Pr}$  values) when modeling rough-wall flows without the need to explicitly adjust model coefficients for roughness or add additional treatment of the dispersive scalar fluxes. Of course, a more systematic study including different types of roughness and a wider range of  $\text{Pr}$  would be required.

The timescale ratio  $\mathcal{R}$  is another important quantity for which the effects of roughness are not well understood. In many models it is also assumed to be constant, with an equilibrium value  $\mathcal{R} \approx 0.5$ . This assumption holds away from a wall, but differences can be observed near a solid surface. For a smooth-wall case, it tends to  $\text{Pr}$  at the wall [36], and the near-wall behavior depends strongly on  $\text{Pr}$ . For the rough-wall case, however, the  $\text{Pr}$  dependence is much reduced, and  $\mathcal{R}$  is lower than the corresponding smooth-wall values. Below the roughness centroid  $d$ ,  $\mathcal{R}$  rises rapidly as the base of the roughness is approached. The location at which this sharp rise starts depends on  $\text{Pr}$ : where for  $\text{Pr} = 1.0$  it happens right under the centroid, for  $\text{Pr} = 0.71$  occurs well below the centroid, most likely due to the fact that the turbulent motions, and, therefore, the turbulent timescales, decay at different distance from the base of the roughness for different scalars due to the dominance of the diffusivity there. Away from the wall, Townsend's similarity hypothesis applies to  $\mathcal{R}$ . The approximation  $\mathcal{R} \approx 0.5$ , which was inaccurate near a smooth wall, is also inaccurate in the rough-wall case, although to a lesser degree. The near-wall behavior appears to be much simpler for a rough wall with a much lower dependence on  $\text{Pr}$ .

In previous work [47], the similarities and differences between the budgets of  $\langle \overline{u'u'} \rangle_s$  and  $\mathcal{K}_\theta = \langle \overline{\theta'\theta'} \rangle_s$  were examined, and it was found that the form-induced (FI) production is dominant for the scalar variance. Here, we considered the budget of turbulent kinetic energy (TKE),  $\mathcal{K}$ , and compared it to the  $\mathcal{K}_\theta$  one. Once again, the FI production  $\mathcal{P}^{FI}$  was much more dominant in the  $\mathcal{K}_\theta$  budget than in that of  $\mathcal{K}$ ; however, due to the reduced importance of the pressure-work term in  $\mathcal{K}$ , the  $\mathcal{K}$  budget is more similar than that of  $\langle \overline{u'u'} \rangle_s$  to the budget of  $\mathcal{K}_\theta$ . Above the centroid, the production is nearly balanced by dissipation for both  $\mathcal{K}$  and  $\mathcal{K}_\theta$ . This also applies to  $\mathcal{K}_\theta$  under the centroid, but not for  $\mathcal{K}$ . This is of importance for models that use a transport equation for  $\mathcal{K}_\theta$ , as it suggests that a specific near-wall correction for roughness might not be necessary and the underlying equilibrium balance  $\mathcal{P}_\theta \approx \varepsilon_\theta$  can be extended all the way to the boundary.

Finally, the scalar dissipation budget was examined. While important for  $\mathcal{K}_{\theta-\varepsilon_\theta}$  type or more complex models, this budget had not been previously considered for a rough-wall case. It is far more complex than the  $\mathcal{K}_\theta$  budget, containing four different production-of-dissipation terms, and has a complex near-wall behavior for a smooth-wall case. In contrast, the rough-wall behavior is significantly simpler, since many terms decrease in importance. While, for a rough wall, the budget satisfies a  $\mathcal{P}_{\varepsilon_\theta} \approx \varepsilon_{\varepsilon_\theta}$  equilibrium, there are several production-of-dissipation terms that need to be considered. While the turbulent production  $\mathcal{P}_{\varepsilon_\theta}^T$  is about twice as large as the other production terms, it is not dominant on its own. A similar trend of significant increase of  $\mathcal{P}_{\varepsilon_\theta}^T$  (compared to all other production terms) had also been observed in a smooth-wall case when  $\text{Pe} = \text{RePr}$  was increased [52], and an increase of  $\text{Pr}$  had a stronger effect than a comparable increase in  $\text{Re}$ . There could be a correspondence between introducing roughness (without changing  $\text{Pe}$ ) and the increase of  $\text{Pr}$ ; from a modeling point of view, this could result in a roughness correction to those models that use a  $\varepsilon_\theta$  equation.

The roughness significantly enhanced the gradient-production of scalar dissipation  $\mathcal{P}_{\varepsilon_\theta}^G$ , due to the roughness imposing large curvature on the mean scalar isosurfaces and to the creation of large

$\bar{\theta}$  gradients locally. This is caused by the fact that for the rough-wall case,  $\mathcal{P}_{\varepsilon\theta}^G$  was entirely due to FI contributions and was shown to only be significant directly at the roughness surface.

Finally,  $\mathcal{P}_{\varepsilon\theta}^T$  was examined to determine why it becomes much more significant in the roughness sublayer. A breakdown of the term based on the principal strain directions showed that, while roughness induces slightly more dominant compressive strains, it is the improved alignment between the fluctuating scalar gradient  $\nabla\theta'$  and the principal compressive direction of the strain-rate tensor that results in the increase of  $\mathcal{P}_{\varepsilon\theta}^T$ . When the angle between  $\nabla\theta'$  and the principal compressive stresses was  $35^\circ$  or less, a significant increase in  $\mathcal{P}_{\varepsilon\theta}^T$  was observed. Beyond the understating of the underlying physical processes, these results are directly relevant to extending probability density function (PDF)-based models for rough-wall applications.

As was pointed throughout this work, the findings are limited to a small range of Prandtl numbers, around unity, and a single case of  $k$ -type roughness. To get a more generalized understanding and confirmation of these results, a systematic study encompassing (1) different roughness geometries, (2) wider range of Prandtl numbers, and (3) wider range of Reynolds numbers is needed. This type of study will shed light on both the trends and sensitivities associated with the different factors as well as allowing the development of improved models.

### ACKNOWLEDGMENTS

U.P. acknowledges the support from the Natural Science and Engineering Research Council of Canada (NSERC) under the Discovery Grant program. U.P. also acknowledges the support of the Canada Research Chair program. Z.H. acknowledges the support of the Ontario Trillium Scholarship (OTS) provided by the Government of Ontario. This research was enabled in part by computational support provided by Compute Ontario [77] and Compute Canada [78].

### APPENDIX A: BREAKDOWN OF THE PRODUCTION TERMS

When we apply the double-average, the terms become: (1) Gradient production:

$$\begin{aligned}\mathcal{P}_{\varepsilon\theta}^G &= -2\alpha \left\langle \left( u'_i \frac{\partial\theta'}{\partial x_k} \right) \frac{\partial^2 \bar{\theta}}{\partial x_i \partial x_k} \right\rangle_s = \tilde{\mathcal{P}}_{\varepsilon\theta}^G - 2\alpha \left\langle v' \frac{\partial\theta'}{\partial y} \right\rangle_s \frac{d^2 \langle \bar{\theta} \rangle}{dy^2}, \\ \tilde{\mathcal{P}}_{\varepsilon\theta}^G &= -\alpha \left\langle \left( u'_i \frac{\partial\theta'}{\partial x_k} \right) \frac{\partial^2 \tilde{\theta}}{\partial x_i \partial x_k} \right\rangle_s - \alpha \left\langle u'_i \frac{\partial\theta'}{\partial x_k} \right\rangle_s \left\langle \frac{\partial^2 \tilde{\theta}}{\partial x_i \partial x_k} \right\rangle_s.\end{aligned}$$

(2) Mean scalar gradient production:

$$\begin{aligned}\mathcal{P}_{\varepsilon\theta}^{\text{MS}} &= -2\alpha \left\langle \left( \frac{\partial u'_i}{\partial x_k} \frac{\partial\theta'}{\partial x_k} \right) \frac{\partial \bar{\theta}}{\partial x_i} \right\rangle_s = \tilde{\mathcal{P}}_{\varepsilon\theta}^{\text{MS}} - 2\alpha \left\langle \frac{\partial v'}{\partial x_k} \frac{\partial\theta'}{\partial x_k} \right\rangle_s \frac{d \langle \bar{\theta} \rangle_s}{dy}, \\ \tilde{\mathcal{P}}_{\varepsilon\theta}^{\text{MS}} &= -\alpha \left\langle \left( \frac{\partial u'_i}{\partial x_k} \frac{\partial\theta'}{\partial x_k} \right) \frac{\partial \tilde{\theta}}{\partial x_i} \right\rangle_s.\end{aligned}$$

(3) Mean velocity gradient production:

$$\begin{aligned}\mathcal{P}_{\varepsilon\theta}^{\text{MV}} &= -2\alpha \left\langle \left( \frac{\partial\theta'}{\partial x_k} \frac{\partial\theta'}{\partial x_i} \right) \frac{\partial \bar{u}_i}{\partial x_k} \right\rangle_s = \tilde{\mathcal{P}}_{\varepsilon\theta}^{\text{MV}} - 2\alpha \left\langle \frac{\partial\theta'}{\partial x} \frac{\partial\theta'}{\partial y} \right\rangle_s \frac{d \langle \bar{u} \rangle_s}{dy}, \\ \tilde{\mathcal{P}}_{\varepsilon\theta}^{\text{MV}} &= -\alpha \left\langle \left( \frac{\partial\theta'}{\partial x_i} \frac{\partial\theta'}{\partial x_k} \right) \frac{\partial \tilde{u}_i}{\partial x_k} \right\rangle_s.\end{aligned}$$



(4) Turbulent production:

$$\mathcal{P}_{\varepsilon\theta}^T = -\alpha \left\langle \frac{\partial\theta'}{\partial x_k} \frac{\partial\theta'}{\partial x_i} \frac{\partial u'_i}{\partial x_k} \right\rangle_s.$$

(5) Turbulent transport:

$$\mathcal{T}_{\varepsilon\theta} = -\alpha \left\langle \frac{\partial}{\partial x_i} \left( u'_i \frac{\partial\theta'}{\partial x_k} \frac{\partial\theta'}{\partial x_k} \right) \right\rangle_s = -\alpha \frac{d}{dy} \left\langle v' \frac{\partial\theta'}{\partial x_k} \frac{\partial\theta'}{\partial x_k} \right\rangle_s.$$

(6) Mean transport:

$$\mathcal{A}_{\varepsilon\theta} = -\alpha \left\langle \frac{\partial}{\partial x_i} \left( \bar{u}_i \frac{\partial\theta'}{\partial x_k} \frac{\partial\theta'}{\partial x_k} \right) \right\rangle_s = \tilde{\mathcal{A}}_{\varepsilon\theta} = -\alpha \frac{d}{dy} \left\langle \tilde{v} \left( \frac{\partial\theta'}{\partial x_k} \frac{\partial\theta'}{\partial x_k} \right) \right\rangle_s.$$

(7) Molecular diffusion:

$$\begin{aligned} \mathcal{D}_{\varepsilon\theta} &= \alpha^2 \left\langle \frac{\partial^2}{\partial x_i \partial x_i} \left( \frac{\partial\theta'}{\partial x_k} \frac{\partial\theta'}{\partial x_k} \right) \right\rangle_s = \tilde{\mathcal{D}}_{\varepsilon\theta} + \alpha^2 \frac{d^2}{dy^2} \left\langle \frac{\partial\theta'}{\partial x_k} \frac{\partial\theta'}{\partial x_k} \right\rangle_s, \\ \tilde{\mathcal{D}}_{\varepsilon\theta} &= \alpha^2 \left\langle \frac{\partial^2}{\partial x_i \partial x_i} \left( \frac{\partial\theta'}{\partial x_k} \frac{\partial\theta'}{\partial x_k} \right) \right\rangle_s. \end{aligned}$$

(8) Molecular dissipation:

$$\varepsilon_{\varepsilon\theta} = -2\alpha^2 \left\langle \frac{\partial^2\theta'}{\partial x_i \partial x_k} \frac{\partial^2\theta'}{\partial x_i \partial x_k} \right\rangle_s.$$

(9) Source-term contribution:

$$\mathcal{Q}_{\varepsilon\theta} = 2\alpha \frac{d\langle T_w \rangle}{dx} \left\langle \frac{\partial\theta'}{\partial x_k} \frac{\partial u'_1}{\partial x_k} \right\rangle_s.$$

## APPENDIX B: TURBULENT PRANDTL NUMBER CALCULATION FOR THE CHANNEL CASE

The turbulent Prandtl number  $\text{Pr}_T$  is the ratio between the eddy viscosity  $\nu_T$  and eddy diffusivity  $\alpha_T$ , as defined in Eq. (10). Contracting Eq. (8) with the time-averaged strain tensor  $S_{ij}$  and scalar gradient  $G_k$ , respectively, yields

$$-\langle \bar{u}'_i \bar{u}'_j \rangle_s \langle \bar{S}_{ij} \rangle_s + \frac{2\mathcal{K}}{3} \delta_{ij} \langle \bar{S}_{ij} \rangle_s = 2\nu_T \langle \bar{S}_{ij} \rangle_s \langle \bar{S}_{ij} \rangle_s \quad (\text{B1})$$

and

$$-\langle \bar{\theta}' u'_k \rangle_s \langle \bar{G}_k \rangle_s = \alpha_T \langle \bar{G}_k \rangle_s \langle \bar{G}_k \rangle_s. \quad (\text{B2})$$

In channel flow, only  $\langle \bar{S}_{12} \rangle_s$ ,  $\langle \bar{S}_{21} \rangle_s$ , and  $\langle \bar{G}_2 \rangle_s$  are nonzero, since superficial averages are considered (the same does not apply to time-averaged terms).

Equations (B1) and (B2) then simplify to

$$\nu_T = -\langle \bar{u}' v' \rangle_s \left[ \frac{d\langle \bar{u} \rangle_s}{dy} \right]^{-1}, \quad \alpha_T = -\langle \bar{\theta}' v' \rangle_s \left[ \frac{d\langle \bar{\theta} \rangle_s}{dy} \right]^{-1}. \quad (\text{B3})$$

Employing these relationships in the definition of  $\text{Pr}_T$ , we obtain Eq. (10). Similarly, repeating the process while including the dispersive terms  $\tilde{u}_i \tilde{u}_j$  and  $\tilde{\theta} \tilde{u}_k$  yields  $\text{Pr}_{T,\text{eff}}$  as shown in Eq. (16).

- 
- [1] J. Jiménez, Turbulent flows over rough walls, *Annu. Rev. Fluid Mech.* **36**, 173 (2004).
- [2] P. Spalart and S. Allmaras, A one-equation turbulence model for aerodynamic flows, in *Proceedings of the 30th Aerospace Sciences Meeting and Exhibit* (AIAA, 1992), p. 439.
- [3] W. P. Jones and B. E. Launder, The prediction of laminarization with a two-equation model of turbulence, *Int. J. Heat Mass Transf.* **15**, 301 (1972).
- [4] D. C. Wilcox *et al.*, *Turbulence Modeling for CFD*, Vol. 2 (DCW Industries, La Canada, CA, 1998).
- [5] D. C. Wilcox, Reassessment of the scale-determining equation for advanced turbulence models, *AIAA J.* **26**, 1299 (1988).
- [6] B. E. Launder, G. Reece, Jr., and W. Rodi, Progress in the development of a Reynolds-stress turbulence closure, *J. Fluid Mech.* **68**, 537 (1975).
- [7] P. A. Durbin, G. Medic, J.-M. Seo, J. K. Eaton, and S. Song, Rough wall modification of two-layer  $k$ - $\epsilon$ , *J. Fluids Eng.* **123**, 16 (2001).
- [8] T. J. Craft, S. E. Gant, H. Iacovides, and B. E. Launder, A new wall function strategy for complex turbulent flows, *Numer. Heat Transf., Part B: Fundam.* **45**, 301 (2004).
- [9] Y. Kuwata and Y. Kawaguchi, Statistical discussions on skin frictional drag of turbulence over randomly distributed semispheres, *Int. J. Adv. Eng. Sci. Appl. Math.* **10**, 263 (2018).
- [10] Y. Kuwata, K. Suga, and Y. Kawaguchi, An extension of the second moment closure model for turbulent flows over macro rough walls, *Int. J. Heat Fluid Flow* **77**, 186 (2019).
- [11] V. Nikora, S. McLean, S. Coleman, D. Pokrajac, I. McEwan, L. Campbell, J. Aberle, D. Clunie, and K. Koll, Double-averaging concept for rough-bed open-channel and overland flows: Applications, *J. Hydraul. Eng.* **133**, 884 (2007).
- [12] M. R. Raupach and R. H. Shaw, Averaging procedures for flow within vegetation canopies, *Boundary-Layer Meteorol* **22**, 79 (1982).
- [13] M. S. Youssef, Y. Nagano, and M. Tagawa, A two-equation heat transfer model for predicting turbulent thermal fields under arbitrary wall thermal conditions, *Int. J. Heat Mass Transf.* **35**, 3095 (1992).
- [14] K. Abe, T. Kondoh, and Y. Nagano, A new turbulence model for predicting fluid flow and heat transfer in separating and reattaching flows—II. Thermal field calculations, *Int. J. Heat Mass Transf.* **38**, 1467 (1995).
- [15] N. Shikazono and N. Kasagi, Second-moment closure for turbulent scalar transport at various Prandtl numbers, *Int. J. Heat Mass Transf.* **39**, 2977 (1996).
- [16] W. M. Kays, Turbulent Prandtl number: Where are we? *ASME Trans. J. Heat Transf.* **116**, 284 (1994).
- [17] S. B. Pope, *Turbulent Flows* (Cambridge University Press, Cambridge, 2001).
- [18] H. Abe, R. Anthony Antonia, and H. Kawamura, Correlation between small-scale velocity and scalar fluctuations in a turbulent channel flow, *J. Fluid Mech.* **627**, 1 (2009).
- [19] R. A. Antonia, H. Abe, and H. Kawamura, Analogy between velocity and scalar fields in a turbulent channel flow, *J. Fluid Mech.* **628**, 241 (2009).
- [20] F. Alcántara-Ávila, S. Hoyas, and M. J. Pérez-Quiles, Dns of thermal channel flow up to  $Re\tau = 2000$  for medium to low Prandtl numbers, *Int. J. Heat Mass Transf.* **127**, 349 (2018).
- [21] R. A. Antonia and J. Kim, Turbulent Prandtl number in the near-wall region of a turbulent channel flow, *Int. J. Heat Mass Transf.* **34**, 1905 (1991).
- [22] Y. Nagano and C. Kim, A two-equation model for heat transport in wall turbulent shear flows, *J. Heat Tran.* **110**, 583 (1988).
- [23] F. Chedevigne, A double-averaged Navier-Stokes  $k$ - $\omega$  turbulence model for wall flows over rough surfaces with heat transfer, *J. Turbul.* **22**, 713 (2021).
- [24] M. C. Silva, L. C. De Lima, and R. F. Miranda, Comparative analysis of different models for the turbulent Prandtl number, *J. Heat Transfer* **121**, 473 (1999).
- [25] T. Cebeci, A model for eddy conductivity and turbulent Prandtl number, *J. Heat Transf.* **95**, 227 (1973).
- [26] J. Kim and P. Moin, Transport of passive scalars in a turbulent channel flow, in *Turbulent Shear Flows 6* (Springer, Berlin, 1989), pp. 85–96.
- [27] S. Pirozzoli, M. Bernardini, and P. Orlandi, Passive scalars in turbulent channel flow at high Reynolds number, *J. Fluid Mech.* **788**, 614 (2016).

- [28] K. Katoh, K.-S. Choi, and T. Azuma, Heat-transfer enhancement and pressure loss by surface roughness in turbulent channel flows, *Int. J. Heat Mass Transf.* **43**, 4009 (2000).
- [29] J. P. Crimaldi, J. R. Koseff, and S. G. Monismith, A mixing-length formulation for the turbulent Prandtl number in wall-bounded flows with bed roughness and elevated scalar sources, *Phys. Fluids* **18**, 095102 (2006).
- [30] S. Leonardi, P. Orlandi, L. Djenidi, and R. A. Antonia, Heat transfer in a turbulent channel flow with square bars or circular rods on one wall, *J. Fluid Mech.* **776**, 512 (2015).
- [31] M. MacDonald, N. Hutchins, and D. Chung, Roughness effects in turbulent forced convection, *J. Fluid Mech.* **861**, 138 (2019).
- [32] J. W. R. Peeters and N. D. Sandham, Turbulent heat transfer in channels with irregular roughness, *Int. J. Heat Mass Transf.* **138**, 454 (2019).
- [33] Y. Kuwata, Direct numerical simulation of turbulent heat transfer on the Reynolds analogy over irregular rough surfaces, *Int. J. Heat Fluid Flow* **92**, 108859 (2021).
- [34] J. R. Ristorcelli, Passive scalar mixing: Analytic study of timescale ratio, variance, and mix rate, *Phys. Fluids* **18**, 075101 (2006).
- [35] C. Beguier, I. Dekeyser, and B. E. Launder, Ratio of scalar and velocity dissipation timescales in shear flow turbulence, *Phys. Fluids* **21**, 307 (1978).
- [36] H. Kawamura, K. Ohsaka, H. Abe, and K. Yamamoto, Dns of turbulent heat transfer in channel flow with low to medium-high Prandtl number fluid, *Int. J. Heat Fluid Flow* **19**, 482 (1998).
- [37] E. Ivanova, Numerical simulations of turbulent mixing in complex flows. PhD. thesis, Universität Stuttgart, Prüfungstermin Juli (2012).
- [38] C.-M. Hogstrom, S. Wallin, and A. V. Johansson, Passive scalar flux modeling for CFD, in *Proceedings of the 2nd Symposium on Turbulence and Shear Flow Phenomena* (Begel House, Inc., Danbury, CT, 2001).
- [39] H. Kolla, J. W. Rogerson, N. Chakraborty, and N. Swaminathan, Scalar dissipation rate modeling and its validation, *Combust. Sci. Technol.* **181**, 518 (2009).
- [40] A. Ashrafian and H. I. Andersson, The structure of turbulence in a rod-roughened channel, *Int. J. Heat Fluid Flow* **27**, 65 (2006).
- [41] J. Yuan and U. Piomelli, Roughness effects on the Reynolds stress budgets in near-wall turbulence, *J. Fluid Mech.* **760**, R1 (2014).
- [42] J. Yuan and J. M. Aghaei, Topographical effects of roughness on turbulence statistics in roughness sublayer, *Phys. Rev. Fluids* **3**, 114603 (2018).
- [43] K. Papadopoulos, V. Nikora, B. Vowinkel, S. Cameron, R. Jain, M. Stewart, C. Gibbins, and J. Fröhlich, Double-averaged kinetic energy budgets in flows over mobile granular beds: Insights from DNS data analysis, *J. Hydraul. Res.* **58**, 653 (2020).
- [44] P. A. Coppin and M. R. Raupach, Measurement of scalar transport in a model plant canopy, in *Proceedings of the 8th Australasian Fluid Mechanics Conference* (University of Newcastle, Australia, 1983), p. 1.
- [45] Y. Miyake, K. Tsujimoto, and M. Nakaji, Direct numerical simulation of rough-wall heat transfer in a turbulent channel flow, *Int. J. Heat Fluid Flow* **22**, 237 (2001).
- [46] Y. Nagano, H. Hattori, and T. Houra, Dns of velocity and thermal fields in turbulent channel flow with transverse-rib roughness, *Int. J. Heat Fluid Flow* **25**, 393 (2004).
- [47] Z. Hantsis and U. Piomelli, Roughness effects on scalar transport, *Phys. Rev. Fluids* **5**, 114607 (2020).
- [48] R. Borghi, Turbulent premixed combustion: Further discussions on the scales of fluctuations, *Combust. Flame* **80**, 304 (1990).
- [49] K. K. Nomura and S. E. Elghobashi, Mixing characteristics of an inhomogeneous scalar in isotropic and homogeneous sheared turbulence, *Phys. Fluids* **4**, 606 (1992).
- [50] T. Mantel and R. Borghi, A new model of premixed wrinkled flame propagation based on a scalar dissipation equation, *Combust. Flame* **96**, 443 (1994).
- [51] N. Chakraborty, J. W. Rogerson, and N. Swaminathan, *A priori* assessment of closures for scalar dissipation rate transport in turbulent premixed flames using direct numerical simulation, *Phys. Fluids* **20**, 045106 (2008).

- [52] F. Alcántara-Ávila and S. Hoyas, Direct numerical simulation of thermal channel flow for medium-high Prandtl numbers up to  $Re_\tau = 2000$ , *Int. J. Heat Mass Transf.* **176**, 121412 (2021).
- [53] N. Kasagi, Y. Tomita, and A. Kuroda, Direct numerical simulation of passive scalar field in a turbulent channel flow, *J. Heat Tran.* **114**, 598 (1992).
- [54] P. Foroughi, M. Stripf, and B. Frohnäpfel, A systematic study of turbulent heat transfer over rough walls, *Int. J. Heat Mass Transf.* **127**, 1157 (2018).
- [55] A. Scotti, Direct numerical simulation of turbulent channel flows with boundary roughened with virtual sandpaper, *Phys. Fluids* **18**, 031701 (2006).
- [56] M. Lee and R. D. Moser, Direct numerical simulation of turbulent channel flow up to  $Re_\tau \approx 5200$ , *J. Fluid Mech.* **774**, 395 (2015).
- [57] S. Hoyas and J. Jiménez, Scaling of the velocity fluctuations in turbulent channels up to  $re \tau = 2003$ , *Phys. Fluids* **18**, 011702 (2006).
- [58] J. Jiménez and P. Moin, The minimal flow unit in near-wall turbulence, *J. Fluid Mech.* **225**, 213 (1991).
- [59] M. MacDonald, D. Chung, N. Hutchins, L. Chan, A. Ooi, and R. García-Mayoral, The minimal-span channel for rough-wall turbulent flows, *J. Fluid Mech.* **816**, 5 (2017).
- [60] A. A. Townsend, *The Structure of Turbulent Shear Flow* (Cambridge University Press, Cambridge/New York, 1976).
- [61] K. A. Flack, M. P. Schultz, and T. A. Shapiro, Experimental support for Townsend's Reynolds number similarity hypothesis on rough walls, *Phys. Fluids* **17**, 035102 (2005).
- [62] K. A. Flack and M. P. Schultz, Roughness effects on wall-bounded turbulent flows, *Phys. Fluids* **26**, 101305 (2014).
- [63] P. S. Jackson, On the displacement height in the logarithmic velocity profile, *J. Fluid Mech.* **111**, 15 (1981).
- [64] P. R. Spalart and Michael Kh. Strelets, Mechanisms of transition and heat transfer in a separation bubble, *J. Fluid Mech.* **403**, 329 (2000).
- [65] G. Grötzbach, Challenges in low-Prandtl number heat transfer simulation and modeling, *Nucl. Eng. Des.* **264**, 41 (2013).
- [66] X. Wu, P. Moin, J. M. Wallace, J. Skarda, A. Lozano-Durán, and J.-P. Hickey, Transitional–turbulent spots and turbulent–turbulent spots in boundary layers, *Proc. Natl. Acad. Sci. USA* **114**, E5292 (2017).
- [67] H. Abe, H. Kawamura, and Y. Matsuo, Surface heat-flux fluctuations in a turbulent channel flow up to  $Re_\tau = 1020$  with  $Pr = 0.025$  and  $0.71$ , *Int. J. Heat Fluid Flow* **25**, 404 (2004).
- [68] H. Abe and R. Anthony Antonia, Scaling of normalized mean energy and scalar dissipation rates in a turbulent channel flow, *Phys. Fluids* **23**, 055104 (2011).
- [69] R. J. Volino, M. P. Schultz, and K. A. Flack, Turbulence structure in rough- and smooth-wall boundary layers, *J. Fluid Mech.* **592**, 263 (2007).
- [70] G. R. Ruetsch and M. R. Maxey, The evolution of small-scale structures in homogeneous isotropic turbulence, *Phys. Fluids* **4**, 2747 (1992).
- [71] P. Vedula, P. K. Yeung, and R. O. Fox, Dynamics of scalar dissipation in isotropic turbulence: A numerical and modeling study, *J. Fluid Mech.* **433**, 29 (2001).
- [72] M. Gonzalez, Analysis of scalar dissipation in terms of vorticity geometry in isotropic turbulence, *J. Turbul.* **13**, N41 (2012).
- [73] W. Wu, U. Piomelli, and J. Yuan, Turbulence statistics in rotating channel flows with rough walls, *Int. J. Heat Fluid Flow* **80**, 108467 (2019).
- [74] S. B. Pope, Pdf methods for turbulent reactive flows, *Prog. Energy Combust. Sci.* **11**, 119 (1985).
- [75] R. O. Fox, The lagrangian spectral relaxation model of the scalar dissipation in homogeneous turbulence, *Phys. Fluids* **9**, 2364 (1997).
- [76] K. Koeltzsch, The height dependence of the turbulent schmidt number within the boundary layer, *Atmos. Environ.* **34**, 1147 (2000).
- [77] [www.computeontario.ca](http://www.computeontario.ca).
- [78] [www.computecanada.ca](http://www.computecanada.ca).